NMR in Biomedicine

WILEY

NMR IN BIOMEDICINE

RESEARCH ARTICLE

ISDU-QSMNet: Iteration Specific Denoising With Unshared Weights for Improved QSM Reconstruction

Venkatesh Vaddadi[1] | Raji Susan Mathew[2] | Phaneendra K. Yalavarthy[1]

[1]Department of Computational and Data Sciences, Indian Institute of Science, Bangalore, Karnataka, India | [2]School of Data Science, Indian Institute of Science Education and Research, Thiruvananthapuram, Kerala, India

Correspondence: Phaneendra K. Yalavarthy (yalavarthy@iisc.ac.in)

Received: 6 November 2024 | **Revised:** 5 August 2025 | **Accepted:** 18 September 2025

Funding: This work was supported by the S. Ramachandran-National Bioscience Award for Career Development awarded by the Department of Biotechnology, Govt. of India, and in part by an ARG Grant# ARG01-0524-230330 from the Qatar National Research Fund (a member of the Qatar Foundation).

Keywords: dipole inversion | inverse problem | model-based deep learning | susceptibility reconstruction

ABSTRACT

Quantitative susceptibility mapping (QSM) estimates the tissue magnetic susceptibility from magnetic resonance (MR) phase measurements by solving an inverse problem. This study introduces iteration specific denoising via unshared weights for QSM reconstruction, also referred to as ISDU-QSMNet, an end-to-end model-based deep learning framework designed to effectively solve the inverse problem of QSM reconstruction from the local field. ISDU-QSMNet introduces significant modifications to existing model-based deep learning approaches by incorporating unshared denoiser weights and random subset sampling during training, leading to a more powerful, robust, and training-efficient model that improves the performance with full training data, reduces the overall training time, and effectively handles different datasets. The proposed method was evaluated against other model-based deep learning approaches, such as learned proximal networks for QSM reconstruction (LPCNN) and Schatten p-norm driven regularizer-based QSM reconstruction (SpiNet-QSM), as well as pure deep learning methods, such as QSMnet, DeepQSM, and xQSM, by performing reconstructions on 94 imaging volumes with varying acquisition parameters under two scenarios: full training data and limited training data. In the full training data scenario, the proposed approach demonstrated substantial improvements over all existing methods in both model-based and pure deep learning categories, achieving significant reductions in high-frequency error norm (HFEN) by up to 3.5% across 60 data volumes. In the limited training data scenario, the proposed approach matched the performance of state-of-the-art model-based deep learning models. Additionally, it demonstrated strong generalization capabilities by effectively handling data with different acquisition parameters and consistently performed well in ROI analysis.

1 | Introduction

Quantitative susceptibility mapping (QSM) is an advanced MRI technique that estimates the magnetic susceptibility of tissues using the measured phase data from three-dimensional (3D) or two dimensional (2D) multislice gradient echo (GRE) acquisitions [1–4]. QSM has several important clinical applications [5–7], particularly in neuroimaging, as it offers both visualization and quantification of tissue susceptibility. It effectively differentiates hemorrhage (paramagnetic, high contrast) from calcifications (diamagnetic, low contrast), visualizes and quantifies brain iron deposits, which are crucial in studying neurodegenerative diseases [6] such as Parkinson's [8,9] and Alzheimer's [10–13], and multiple sclerosis [14–16]. QSM is a valuable tool for studying microstructural and compositional changes in the brain associated with various neurological conditions, with applications

in improving diagnostic precision, guiding treatment planning, and facilitating disease monitoring. The susceptibility map is generated through a multistep process involving phase unwrapping to resolve 2π ambiguities, background field removal to obtain the local field map, and dipole inversion to reconstruct the final susceptibility distribution. Additional postprocessing details are provided in the supplementary materials. Inversion is an ill-conditioned problem because the dipole kernel has zeroes along a conical surface and, therefore, undersamples k-space, calling for either handcrafted or learned priors for accurate map reconstruction [17].

Traditional iterative QSM reconstruction methods, such as morphology-enabled dipole inversion (MEDI) [18] and fast nonlinear susceptibility inversion with variational regularization (FANSI) [19] utilize iterative algorithms with handcrafted regularizers. FANSI [19] is a nonlinear QSM algorithm that employs variable splitting and the alternating direction method of multipliers (ADMM). This approach decomposes the problem into simpler subproblems with closed-form solutions, while the decoupled nonlinear inversion is solved using a Newton–Raphson iterative scheme. However, the resulting image quality is highly sensitive to the choice of the regularization parameter, which controls the trade-off between data fidelity and image smoothness. Alternatively, in nonlinear dipole inversion (NDI) [20] method, optimization solely performed on the nonlinear forward model without explicitly introducing a regularization term, and solving it using a simple gradient descent rule. These approaches, although effective to an extent, often struggle to balance the trade-off between image fidelity and noise suppression, and their performance can be significantly affected by the choice of regularization parameters or the number of iterations used in the reconstruction.

In recent years, deep learning has significantly affected medical imaging by providing data-driven solutions (end-to-end deep learning methods) that learn complex mappings directly from data. Convolutional neural networks (CNNs) have shown promising results in QSM reconstruction. Examples include QSMnet, DeepQSM, and xQSM, which use deep neural networks to map single-orientation phase measurements to multiorientation calculation of susceptibility through multiple-orientation sampling (COSMOS) [21] susceptibility maps. QSMnet [22] employs a 3D CNN UNet [23] architecture, DeepQSM [24] uses synthetic data to learn the physical forward problem, and xQSM [25] introduces octave convolutions to enhance the QSM reconstruction performance, which requires end-to-end training from the local field to COSMOS. However, these methods do not incorporate the underlying physics of the QSM problem, making them more biased towards the training data and less adaptable to changes in the input distributions. To address this, model-based deep-learning (MoDL) approaches have been developed that combine the strengths of deep learning with the underlying physics of the problem [26].

To addresses the challenges in QSM reconstruction arising from varying acquisition orientations and anisotropic voxel sizes, Xiong et al. proposed AFTER-QSM (Affine Transformation Edited and Refined Deep Neural Network for quantitative susceptibility mapping), which is a model-based deep learning method. The method incorporates affine transformations to align images into a consistent coordinate space, followed by a U-Net architecture for dipole inversion and a residual dense network for refinement, enhancing generalizability across diverse imaging conditions [27]. Notably, Graf et al. [28] proposed an adaptive convolutional network that integrates a prior information about imaging parameters, such as orientation and resolution, into the reconstruction process to improve generalizability. Similarly, adaptive instance normalization (AdaIN)-QSM by Oh et al. [29] applies AdaIN to address performance degradation due to resolution mismatches between training and testing datasets.

Alternatively, there are single step QSM reconstruction methods like Instant QSM (iQSM), which is a deep learning-based method that enables near-instant quantitative susceptibility mapping directly from raw MRI phase data by bypassing traditional multistep processes, significantly reducing reconstruction time and improving accuracy [30]. iQSM+ further enhanced this framework by integrating a novel orientation-adaptive latent feature editing (OA-LFE) module to enable accurate, artifact-reduced reconstructions across arbitrary dipole field orientations, demonstrating superior performance over existing DL-QSM methods [31].

Meanwhile, all the aforementioned methods perform dipole deconvolution in a single step, by directly computing QSM from the input local field. However, two-step methods exist, such as data fidelity–based QSM (DF-QSM) [32], fidelity imposed network edit (FINE) [33], and model-resolution-based deconvolution for improved QSM (MR-QSM) [34]. These methods first predict the QSM from the local field and then refine the prediction in a second step, which incorporates gradients derived from the physics of QSM. These methods often require additional computing and the solution of the initial step to be in close proximity to the target reconstruction. Model-based Deep Image Prior for QSM (MoDIP-QSM) is an unsupervised, training-free method that combines a small untrained neural network with a data fidelity optimization module. The network serves as an implicit prior for image regularization, while the optimization enforces the physical dipole inversion model. MoDIP-QSM has demonstrated improved generalizability and computational efficiency in QSM reconstruction, particularly in handling variations in scan parameters [35]. However, it is important to note that in inverse problems like QSM reconstruction, which involve high-dimensional null spaces, deep image prior (DIP) has limitations in recovering all relevant information. Research on magnetic resonance imaging reconstruction has shown that DIP performs suboptimally, especially when the forward operators are complex or the data are highly undersampled [36]. Furthermore, DIP tends to recover low-frequency components of the image more quickly than high-frequency details, leading to a spectral bias that can result in the loss of fine structural information, which is critical in QSM maps [36–38].

Model-based deep learning techniques have emerged as promising paradigms that combine the strengths of traditional model-based methods and deep learning. By integrating the physical model of the QSM reconstruction problem into the deep learning framework, these techniques aim to leverage the advantages of both the strong prior knowledge encoded in the physical model and the powerful feature-learning capabilities of deep neural

networks. In each iteration, the model-based deep learning uses the predicted QSM from the previous iteration to refine and improve the prediction in the current iteration. Thus, model-based deep learning can be viewed as a multistep refinement process (known as unrolling) for QSM reconstruction. However, the training is performed in an end-to-end fashion.

Learned proximal convolutional neural networks for quantitative susceptibility mapping (LPCNN) [39] and Schatten p-norm regularization for improved quantitative susceptibility mapping (SpiNet-QSM) [40] are examples of approaches developed for QSM reconstruction. LPCNN combines the proximal gradient algorithm with 3D-WideResNet to form an unrolled iterative model. It iteratively refines solutions using a data-driven regularizer through its CNN component, which acts as a proximal operator to enhance the reconstruction quality by learning from data, thereby decoupling the forward model from data-driven parameters. SpiNet-QSM is another iterative unrolled model that utilizes a Schatten p-norm–driven CNN denoiser-based regulariser.

Although the aforementioned model-based deep learning methods effectively integrate the physical principles of the QSM forward model with the representational power of deep neural networks, they remain insufficient to fully address the challenges of QSM reconstruction. These methods generally outperform purely data-driven approaches, particularly in low-data regimes— which is supported by prior studies comparing both paradigms across varying levels of data availability [32, 40]. However, when large amount of training data are available, the performance gap between model-based and pure deep learning methods tends to narrow. The inherent incorporation of model physics gives model-based approaches an advantage in terms of generalizability. Nevertheless, these observations indicate that there remains considerable scope for improving model-based deep learning frameworks, especially in high-data scenarios. With optimized architectural design, such methods could yield superior performance and robustness in QSM reconstruction. Alternatively, another major limitation of existing model-based deep learning techniques is their high computational cost during training, which often compels the use of simplified architectures with fewer unrolling iterations. This trade-off restricts their utility primarily to data-constrained settings and undermines their potential benefits in high-data regimes. Moving toward more efficient training paradigms that reduce computational overhead could enable the adoption of deeper unrolled architectures. This, in turn, would facilitate more effective exploitation of larger training datasets, leading to improved QSM reconstruction performance compared to current methods such as LPCNN [39] and SpiNet-QSM [40].

To overcome the limitations of existing model-based deep learning techniques in QSM reconstruction, we propose a novel approach called Iteration-Specific Denoising with Unshared Weights-QSMNet (ISDU-QSMNet), which introduces an iteration-specific denoiser with unshared weights to improve susceptibility map refinement. By assigning unique weights to each iteration, the network learns denoising parameters tailored to that stage of reconstruction. Unlike shared weight model-based deep learning methods, the design of ISDU-QSMNet supports iteration-specific regularization, improving reconstruction quality progressively. This results in superior QSM reconstruction performance compared to conventional shared-weight approaches. To address the challenge of long training times, ISDU-QSMNet employs random subset sampling. The unshared weights enhance the model's capacity to leverage large datasets, while subset sampling accelerates training without sacrificing accuracy. This design enables efficient, high-quality QSM reconstruction. Extensive evaluations show that ISDU-QSMNet outperforms state-of-the-art methods in both full-data and limited-data scenarios, offering superior performance and generalizability.

2 | Methods

2.1 | Datasets

Five datasets are used in this study. Dataset-I comprises SNU data from Seoul National University, including 60 volumes from 12 healthy subjects, acquired using a 3 T MRI scanner across five head orientations [22]. Dataset-II is the LPCNN data shared by Lai et al. [39], consisting of 32 volumes from eight subjects at 7 T, with varying dimensions. Dataset-III is from reconstruction challenge-1 (RC-1) [41], which includes a single 3 T volume with 12 head orientations. Dataset-IV is from reconstruction challenge-2 (RC-2) [42, 43] and comprises two simulated volumes. Dataset-V is a scanning volume acquired from a subject with hemorrhage on a 3 T MR scanner with different resolution [44]. Further details, including acquisition, resolution and other key parameters, are provided in the supplementary material.

The SNU data were used to train the model. The local field served as the input, while rotated COSMOS maps aligned with the input local field were used as the ground truth. A physics-based data augmentation strategy was applied to increase the training dataset [22]. The COSMOS QSM maps were rotated between -30° and $+30^{\circ}$ relative to the B0 direction, and the corresponding local field maps were generated by convolving the rotated COSMOS maps with the dipole kernel. This approach ensured consistency with the physics of the QSM problem and effectively doubled the size of the training dataset by generating additional COSMOS–local field pairs through each rotation. Training involved generating multiple 3D patches of size $64 \times 64 \times 64$ voxels with a 66% overlap. The COSMOS map was used as the ground truth for all the methods.

2.2 | QSM Reconstruction Model

The QSM reconstruction problem seeks to estimate the susceptibility distribution (χ) from the observed local magnetic field (y). These belong to function spaces X and Y, respectively. The relationship between them can be modeled as:

$$y = f(\chi), \tag{1}$$

where f represents the (typically nonlinear) forward mapping from susceptibility to field, often involving dipole convolution. Because of the presence of zeros in the dipole kernel in the Fourier domain, this forward operator is ill-posed and does not admit a well-defined inverse in the classical sense. In purely

deep learning-based approaches, the reconstruction task is reformulated by learning an approximate inverse mapping $\mathcal{F}_\theta: Y \rightarrow X$, where $\mathcal{F}_\theta \approx f^{-1}$ is a parameterized model trained to estimate χ from y.

A linearized version of the QSM forward model [39] is commonly used, expressed as:

$$\phi\chi = y \tag{2}$$

$\phi = F^H DF$ represents the forward operator, where F denotes the discrete Fourier transform and D refers to a diagonal matrix in the Fourier domain corresponding to the dipole kernel. The entries of D are given by the expression $D(k) = \frac{1}{3} - \frac{k_z^2}{\|k\|^2}$, which vanishes on the conical surface defined by $2k_z^2 = k_x^2 + k_y^2$. This leads to a nontrivial null space, making the direct inversion of D ill-posed or unstable due to the presence of zeros or near-zero values along its diagonal. Consequently, the QSM reconstruction problem becomes an ill-posed inverse problem, necessitating prior knowledge or regularization to stabilize the solution. Model-based deep learning solvers use Equation 2 for the fidelity term and derive the QSM calculations. Unlike direct deep learning models, model-based solvers maintain a linear approximation from Equation 2 to ensure that the solutions adhere to the underlying physics.

2.3 | Model-Based Deep Learning for QSM

In this study, a model-based deep learning framework is used to solve the QSM reconstruction problem by leveraging an iterative unrolled approach commonly used for inverse problems. The QSM-specific implementation of the mode-based deep learning framework is represented by the following equation:

$$\chi^* = \arg\min_{\chi} \left\{ \underbrace{\| \phi\chi - y \|_2^2}_{\text{QSM data consistency}} + \underbrace{\lambda \| \chi - D_w(\chi) \|_2^2}_{\text{Prior Information Enforcing Term}} \right\} \tag{3}$$

In this context, χ represents the susceptibility map, ϕ relates the susceptibility map to the local field y (QSM data consistency term), $D_w(\chi)$ enforces prior information, and λ controls the tradeoff between data fidelity and prior enforcement. The optimization Equation 3 is solved in an unrolled iterative manner using its corresponding normal equations, as detailed in the following equations:

$$\chi_0 = \phi^H y \tag{4}$$

$$z_k = D_w(\chi_{k-1}) \tag{5}$$

$$\chi_k = \left(\phi^H\phi + \lambda_k I\right)^{-1}\left(\phi^H y + \lambda z_k\right) \tag{6}$$

Here, I is the identity matrix. Thus, the iterative process continues for K unrollings, with the training parameters for D_w and λ learned in an end-to-end fashion. To reduce the number of training parameters, the network parameters of D_w and the regularization parameter λ are shared across the unrolls. Equation 6 can be solved by using the conjugate gradient (CG) descent algorithm. This approach effectively bridges deep learning with QSM, enabling accurate susceptibility mapping from the phase data.

2.4 | Proposed ISDU-QSMNet

The proposed ISDU-QSMNet leverages key parameters of model-based deep learning, specifically the unrolling parameter (K), unshared weights, and the subset-sampling parameter (n). By carefully balancing these factors, we can optimize the training efficiency while maintaining a strong performance of the model-based deep learning technique for QSM reconstruction. The following sections provide a detailed exploration of these parameters in the context of the ISDU-QSMNet architecture.

2.4.1 | Unshared Weights

In the ISDU-QSMNet design, the model-based deep learning approach is modified by replacing the CNN-based denoiser with unshared weights rather than using a CNN-based denoiser with shared weights across unrolling iterations. This modification introduced iteration-specific denoisers, each with its own set of training parameters. This means that we are updating the existing model-based deep learning model to include iteration-specific denoisers through unshared weights. Despite this modification, the design still utilizes a CNN denoiser-based regularizer, which is similar to the existing MoDL design. As a result, the regularization parameters (λ_i) are also iteration-specific to effectively implement iteration-specific regularization. This design achieves both iteration-specific denoising and regularization. It also adds flexibility to the model-based deep learning QSM approach and enhances its ability to capture subtle variations in data, especially when dealing with complex features such as susceptibility distributions.

2.4.2 | Unrolling Parameter (K)

The unrolling parameter (K) in the model-based deep-learning technique for QSM represents the number of iterations performed within the end-to-end framework. Essentially, this parameter translates to the number of stages that the model undergoes to refine the susceptibility map. By unrolling the traditional iterative process into K distinct stages within the deep learning model, each stage can be considered as a layer in the neural network. Adjusting K allows us to control the complexity of the model and the degree of refinement applied to the QSM solution.

Generally, a higher K value enhances the capacity of the model, allowing it to capture more detailed features and potentially lead to more accurate reconstructions. In existing MoDL designs with shared-weight denoisers, capacity is constrained by a fixed set of parameters shared across all iterations, which are suitable for smaller datasets. As a result, increasing K does not necessarily enhance the model's capacity, although

it still increases complexity. In contrast, the proposed ISDU-QSMNet design with iteration-specific denoisers through unshared weights does not constrain the capacity of the model. This approach allows for higher K values, effectively enhancing the model's ability to handle more data. Careful consideration was also given to selecting CNN model designs to prevent overfitting and ensure effective model performance. However, it is important to note that using a large K can lead to increased computational costs, making the training process more resource intensive.

2.4.3 | Subset Sampling

The proposed model-based design with a large unrolling parameter (K) and unshared weights is a powerful model for QSM reconstruction. However, training such models can be computationally expensive. To mitigate this, the proposed approach employs subset sampling, in which only a subset of n samples is used for training each epoch. These n samples were randomly selected from the full dataset, ensuring that after a sufficient number of epochs (N), the model was exposed to all available samples. Training with a smaller subset in each epoch significantly reduces computational demands compared to training on the entire dataset simultaneously, leading to faster training times. The size of the subset (n) was chosen based on the dataset characteristics.

2.5 | Mathematical Equations

In this work, we adopted and modified the mathematical formulation from MoDL to solve the QSM reconstruction problem. The following are proposed and modified equations.

$$\chi_0 = \phi^H y \tag{7}$$

$$z_k = D_{W_k}(\chi_{k-1}) \tag{8}$$

$$\chi_k = \arg\min_{\chi} \left\{ \|\phi\chi - y\|_2^2 + \lambda_k \|\chi - z_k\|_2^2 \right\} \tag{9}$$

Equation 9 defines the core optimization framework of ISDU-QSMNet for QSM reconstruction by formulating the objective function to update the susceptibility map χ_k through a balance of data fidelity and regularization. Here, λ_k represents the regularization parameter for the k-th iteration. D_{W_k} represents the iteration-specific CNN-based denoiser at iteration k. The optimization problem is analytically solvable by deriving its normal equations, yielding the closed-form solution given below:

$$\chi_k = \left(\phi^H\phi + \lambda_k I\right)^{-1}\left(\phi^H y + \lambda_k z_k\right) \tag{10}$$

Here, z_k represents the denoised susceptibility map calculated in Equation 8 using an iteration specific CNN denoiser D_{W_k} for the k^{th} iteration. This denoised output z_k is then used in the optimization Equation 9, where the QSM problem is solved with a denoiser-based regularization term. Equation 10 shows how this optimization equation is solved by formulating the normal equations. Equations 8, 9, and 10 together represent a single iteration step of the proposed ISDU-QSMNet. These steps are repeated for K iterations, corresponding to K unrolling iterations.

2.6 | Proposed ISDU-QSMNet Architecture

The proposed ISDU-QSMNet architecture is shown in Figure 1, comprises two primary blocks: a regularizer block and a data consistency block. The regularizer block features a CNN-based denoiser that handles the denoising process as defined in Equation 8. The data consistency block uses a CG method to solve the optimization problem based on normal equations, as defined in Equation 9. In this CG implementation, 25 iterations ($M_1 = 25$) are used to estimate χ given z_k, which is then passed to the next iteration. The denoiser block (D_{w_k}) employs a 3D-WideResNet18 CNN inspired by previous studies [39, 40, 45], serving as a data-driven regularizer through residual learning. It consisted of 21 convolutional layers, including eight residual blocks, with batch normalization and ReLU activation applied within the blocks. The first 17 layers use a $3 \times 3 \times 3$ kernel and the final layers use a $1 \times 1 \times 1$ kernel. The proposed ISDU-QSMNet architecture also utilizes iteration-specific learning parameters to improve performance, represented as $\theta_i = \{\lambda_i, w_i\}_{i=1}^{K}$, where λ_i is the iteration-specific regularization parameter, w_i are the weights of the iteration-specific denoiser, i is the iteration number, and K is the total number of iterations in the unrolled network.

2.6.1 | Optimization Perspective on Iteration-Specific Denoisers in QSM Reconstruction

In the ISDU-QSMNet formulation, D_{W_k} acts as a denoiser, functioning as part of a CNN-based regularizer in the optimization process for QSM reconstruction. Unlike other model-based deep learning algorithms, D_{W_k} is a convolutional neural network (CNN) trained to denoise the susceptibility map χ by leveraging learned prior information. This is reflected in the regularization term $\lambda_k \| \chi - D_{W_k}(\chi) \|_2^2$, which minimizes the difference between the original map and the denoised output. The term $\lambda_k \| \chi - D_{W_k}(\chi) \|_2^2$ plays a crucial role in addressing the ill-posed nature of the QSM problem by enforcing regularization, where the parameter λ_k balances this regularization with data consistency by adapting to the training data at the k-th iteration. This D_{W_k} adapts during training and learning from data to reduce noise while preserving the structural features of the map, making it distinct from traditional fixed-prior methods. To demonstrate the functionality of D_{W_k} as a denoiser, difference maps between the denoised outputs $D_{W_k}(x_k)$ and the COSMOS ground truth susceptibility map (x) are shown for each iteration. These maps illustrate how the denoising process evolves across iterations, with D_{W_k} refining the susceptibility map to align more closely with the ground truth. In Figure 2, the QSM reconstructions for subject 7 were shown using the ISDU-QSMNet model with unshared denoisers. The figure shows reconstructed maps at each iteration (x_0–x_4) with HFEN values, denoised outputs (z_1–z_4), and difference maps ($x_k - z_k$, COSMOS - z_k), highlighting the denoising effect and alignment with the ground truth. The COSMOS $- x_k$ differences further assess the accuracy of the reconstruction across iterations. These visualizations confirm D_{W_k}'s role in refining the susceptibility map.

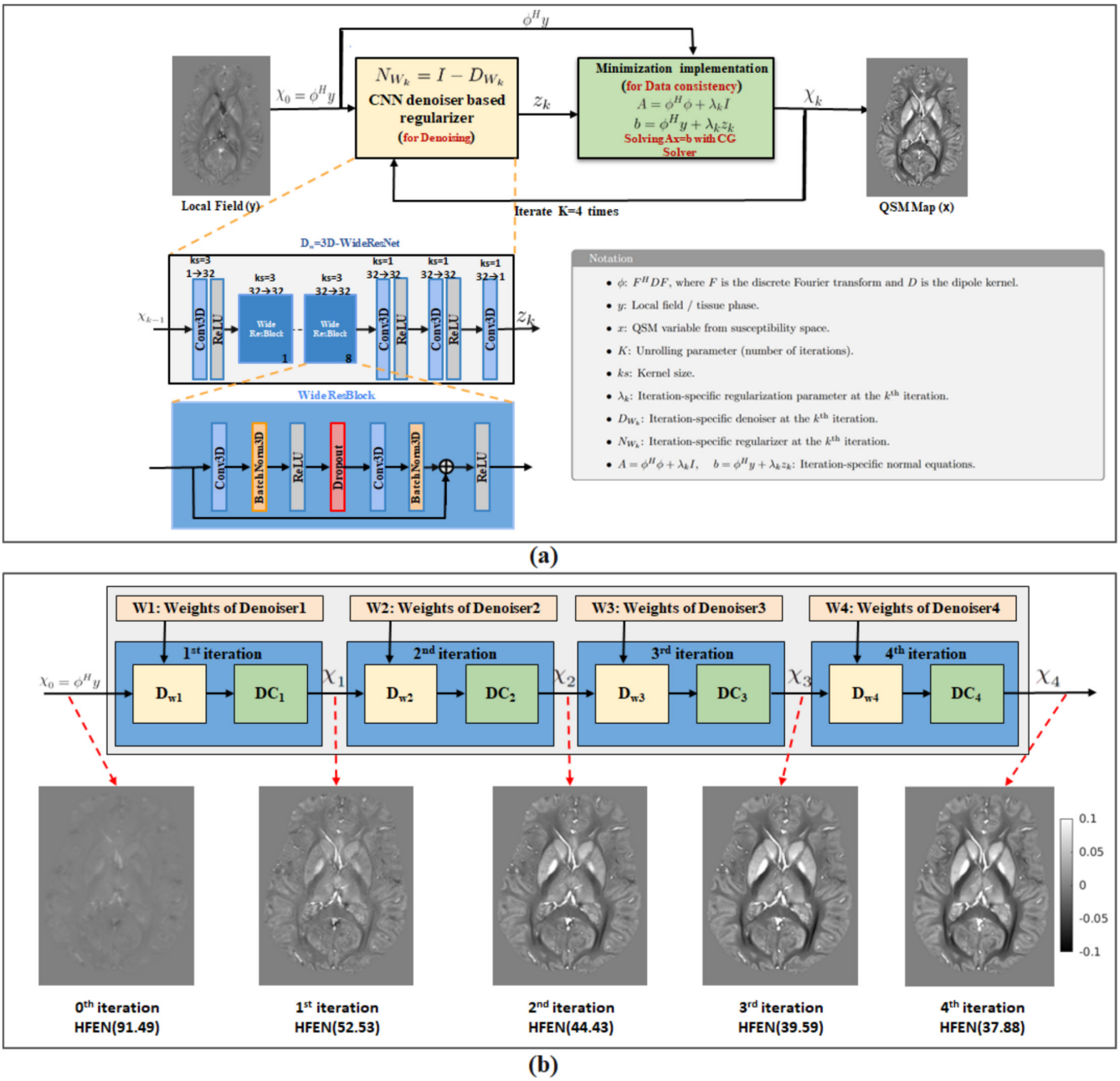

FIGURE 1 | (a) The network architecture of ISDU-QSMNet consists of two blocks per iteration: a CNN-denoiser (D_w) block and a data consistency block. (b) The proposed ISDU-QSMNet is presented as an iterative unrolled architecture with iteration-specific denoisers that use unshared weights. The bottom row shows susceptibility map reconstructions over iterations for subject 7 from SNU dataset, demonstrating progressive refinement. The corresponding high-frequency error norm (HFEN) values relative to COSMOS highlight substantial improvements across iterations.

2.6.2 | Design and Optimization Comparison With LPCNN

The proposed ISDU-QSMNet is a model-based deep learning framework that, like LP-CNN, employs iterative unrolling for QSM reconstruction. While both methods share this architectural foundation, ISDU-QSMNet introduces several key differences that distinguish it from LP-CNN and similar approaches. First, ISDU-QSMNet uses a CNN as a denoiser, which is integrated as part of a regularization term within the optimization framework. In contrast, LP-CNN employs a CNN as a learned proximal operator, which directly serves the role of regularization but in a different mathematical form. Second, ISDU-QSMNet features unshared denoiser weights across iterations, meaning that each unrolling step is having a dedicated CNN tailored specific to that stage. This design enables iteration-specific refinement. On the other hand, LP-CNN uses shared weights across iterations, applying the same CNN parameters for denoising at every step, which limits adaptability. Third, ISDU-QSMNet adopts conjugate gradient descent for solving the data consistency subproblem during each iteration, offering greater computational efficiency. In contrast, LP-CNN uses proximal gradient descent, which is generally less efficient, as also demonstrated in [40].

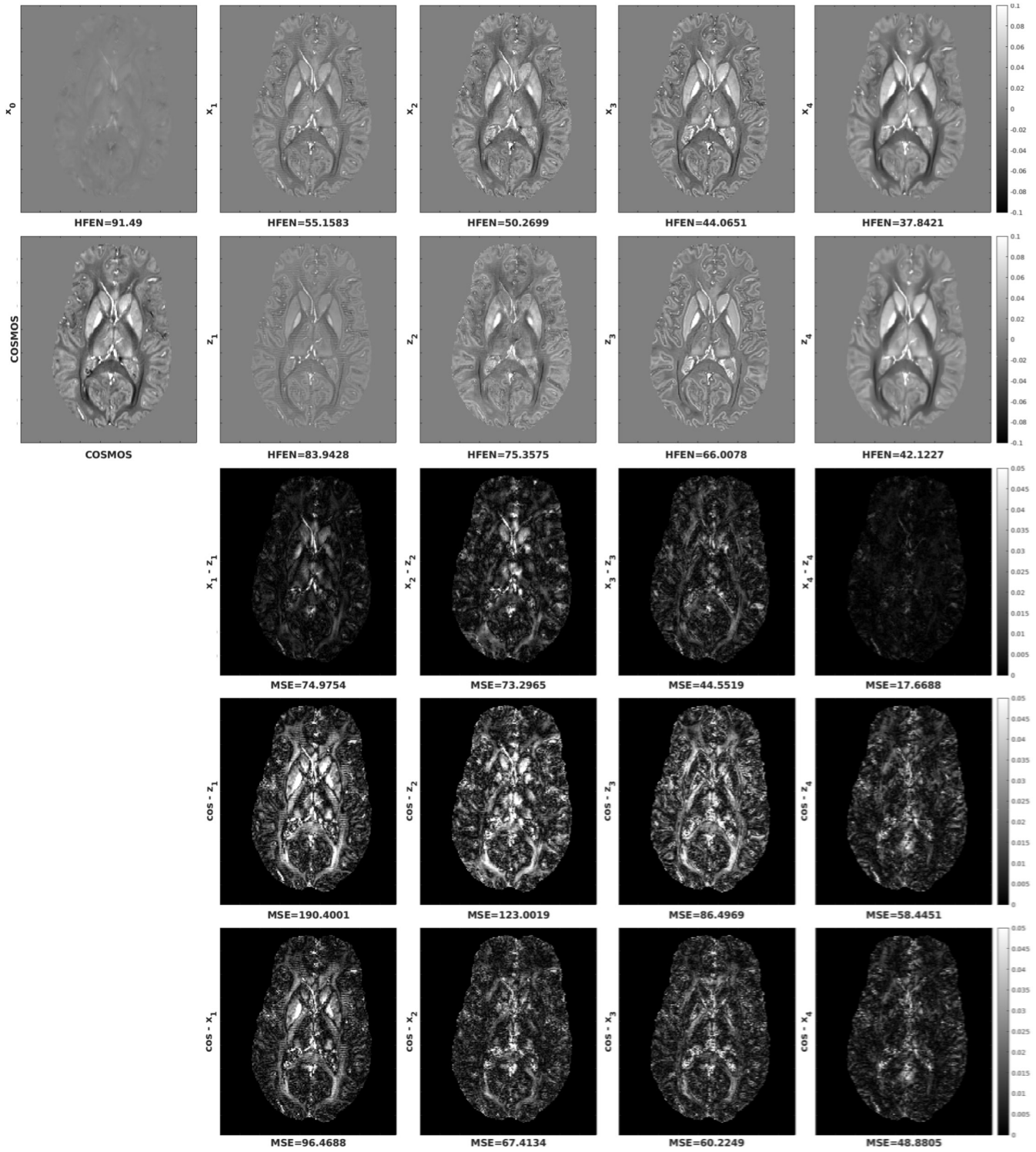

FIGURE 2 | Visualization of intermediate and final QSM reconstructions for subject 7 from the SNU data [22], using the *ISDU-QSMNet* model with unshared denoisers. The first row shows reconstructed susceptibility maps at each unrolled iteration stage (x_0–x_4), annotated with HFEN values relative to the COSMOS ground truth. The second row shows the corresponding denoised outputs (z_1–z_4), with the corresponding HFEN values given below each images. The third and fourth rows display difference maps: ($x_k - z_k$) and (COSMOS $- z_k$), respectively, highlighting the denoising effect and the alignment with ground truth. The last row presents COSMOS $- x_k$ differences indicative of improvements in reconstruction accuracy across iterations.

2.7 | Implementation

The proposed ISDU-QSMNet was implemented using Python 3.10.9 and PyTorch 2.0.1, and trained on an NVIDIA GeForce RTX 3090 GPU. The Adam optimizer was used for all the models. The training parameters, including the learning rate, loss function, batch size, and number of epochs are summarized in Table 1. These parameters were empirically chosen based

TABLE 1 | Summary of training parameters for various models trained on the SNU dataset using the full training data setting, including learning rate, loss function, batch size, and number of training epochs.

Experiment	Learning rate	Loss function	Batch size	No. epochs trained
ISDU-QSMNet, $K=4$	1×10^{-4}	$Loss_{combined}$	2	45
SpiNet-QSM, $K=4$	1×10^{-4}	$Loss_{combined}$	2	45
LP-CNN, $K=3$	1×10^{-4}	$Loss_{combined}$	2	80
QSMNet	5×10^{-4}	$Loss_{combined}$	8	25
Deep QSM	5×10^{-4}	$Loss_{L2}$	8	25
xQSM	5×10^{-4}	$Loss_{L2}$	8	25

on the validation performance. The $loss_{L1}$ term is the l_1-norm of the voxel-wise differences between the reconstructed susceptibility and ground truth COSMOS, whereas the $loss_{Gradient}$ term is the l_1-norm of the gradient differences. Weights $w_1 = 1$, $w_2 = 0.5$, and $w_3 = 0.5$ were chosen empirically. The $loss_{L2}$ term is the l_2-norm of the voxel-wise differences, representing the mean square error between the ground truth and the reconstructed QSM.

$$loss_{combined} = w_1(loss_{L1}) + w_2(loss_{Gradient}) + w_3(loss_{Model}) \quad (11)$$

2.7.1 | Selection of Denoiser D_{W_k}

The primary objective of this study was to develop a model-based deep learning solution for QSM that required an architecture capable of iterative unrolling to progressively refine the QSM map, integrating unshared weights while balancing complexity to prevent overfitting with limited data and underfitting with a full dataset. The selection of the appropriate denoiser D_{W_k} was a crucial step in this process. To this end, we explored various architectures, including a simple residual-learning-based 3D CNN, 3D-UNet, and 3D-WideResNet18 from SpiNet-QSM and LPCNN.

Experiments were conducted using four different CNN architectures to identify the most suitable denoising network: Simple WideResNet CNN, a lightweight model with a single residual connection and 5 layers; UNet-mini, a compact model with 4 encoders and 4 decoders using $3\times3\times3$ filters; UNet-heavy, a more parameterized model with $5\times5\times5$ filters; and WideResNet-18, a ResNet-based model with eight residual connections designed to maintain spatial resolution. Quantitative performance metrics (SSIM, pSNR, NRMSE, HFEN) and computational costs for each network are summarized in Table 2, with sample reconstructions shown in Figure 6 of the supplementary material. These performance metrics clearly demonstrated that WideResNet-18 achieved the best balance between computational efficiency and reconstruction quality, leading to its selection as the denoising network for ISDU-QSMNet.

TABLE 2 | Comparison of different CNN architectures used as denoisers in ISDU-QSMNet, evaluated on the SNU dataset [22] under full training data conditions. The table summarizes the performance of Simple WideResNet CNN, UNet-mini, UNet-heavy, and WideResNet-18 across key metrics including SSIM, pSNR, NRMSE, and HFEN. It also reports the computational cost (in Giga FLOPs) and model size (in millions of parameters). The results show that WideResNet-18, with its balance of computational efficiency and high reconstruction quality, was selected as the denoising network for ISDU-QSMNet.

Model (CNN)	Unrolling parameter (K)	Parameter space (M)	Computation (G.FLops)	SSIM	xSIM	pSNR	NRMSE	HFEN
UNet-mini	1	5.65	286.43	0.905 ± 0.014	0.594 ± 0.038	40.921 ± 0.997	52.289 ± 3.422	50.704 ± 4.391
UNet-mini	4	16.94	859.29	0.908 ± 0.013	0.610 ± 0.034	40.901 ± 1.016	52.256 ± 3.220	51.110 ± 3.706
UNet-heavy	1	99.46	5158.15	0.910 ± 0.014	0.609 ± 0.043	41.267 ± 1.024	50.698 ± 3.794	48.724 ± 4.807
UNet-heavy	4	298.37	15474.45	0.908 ± 0.014	0.608 ± 0.041	41.036 ± 1.029	51.581 ± 3.701	49.858 ± 4.323
WideResNet (simple)	1	0.34	1684.99	0.903 ± 0.016	0.575 ± 0.053	40.689 ± 1.206	53.650 ± 4.310	51.751 ± 4.598
WideResNet (simple)	4	1.02	5054.97	0.907 ± 0.015	0.589 ± 0.051	41.025 ± 1.112	51.778 ± 4.194	49.234 ± 4.729
WideResNet18	1	0.45	2224.17	0.910 ± 0.015	0.599 ± 0.052	41.089 ± 1.188	51.175 ± 4.312	48.608 ± 4.920
WideResNet18	4	1.34	6672.51	0.915 ± 0.014	0.605 ± 0.044	41.368 ± 1.103	50.309 ± 3.865	46.726 ± 5.020

To ensure that the selected WideResNet architecture is the optimal denoising model, an overfitting risk calculation was performed as a hypothesis test to evaluate whether shallower architectures could provide a better balance between model complexity and computational efficiency compared to the chosen WideResNet-18. This test will allow us for assessing whether a simpler model could maintain or improve performance without overfitting, providing a rationale for the final model choice. For that, experiments were conducted by replacing the proposed ISDU-QSMNet's WideResNet-18 architecture with shallower WideResNet models, evaluating their impact on the model's parameter count, computational efficiency, and overall performance. The WideResNet-18 architecture, with its 18-layer depth, demands significant computational resources due to the consistent image size maintained throughout the forward pass. Despite having a relatively modest parameter count (approximately 1.8 M), the computational cost primarily arises from maintaining the original image size, which mimics the behavior of iterative methods. In these experiments, the depth of the WideResNet architecture was varied (with depths of 10, 12, 14, 16, and 18) to evaluate the trade-offs between model complexity and computational efficiency. The results, including performance metrics across different unrolling iterations (K) and WideResNet depths, are presented in Table 3.

Moreover, it is crucial to consider the impact of unshared weights over shared weights. The unshared weights approach in ISDU-QSMNet increases the parameter space by a factor of K compared to model-based deep learning methods with shared weights like LPCNN and SpiNet-QSM. However, the increase in parameter space required by the proposed model is minimal in comparison to existing deep learning models. In the ISDU-QSMNet architecture, unshared weights are utilized in the denoising step, enabling each iteration to independently apply specialized denoising transformations. This approach contrasts with existing model-based deep learning methods that use shared weights, which can limit the model's ability to adapt and refine the denoising process at each iteration. As a result, shared weights reduce the model's flexibility and overall performance, particularly in complex reconstruction tasks like QSM.

However, from a computational complexity perspective, methods that use shared weights do not necessarily result in lower

TABLE 3 | Performance comparison of ISDU-QSMNet variants using WideResNet denoisers of different depths, evaluated under full training data conditions from the SNU dataset [22]. Each row presents results for a specific configuration, with varying model complexities achieved by adjusting both the number of unrolling iterations (K) and the depth of the WideResNet architecture (depths of 10, 12, 14, 16, and 18). All metrics are reported as mean ± standard deviation.

Model	K	No. parameters (M)	Comput. (G.Flop)	SSIM	xSIM	pSNR	NRMSE	HFEN
WideResNet-10	1	0.225	1121.6	0.905 ± 0.015	0.583 ± 0.053	40.858 ± 1.176	52.516 ± 4.324	50.232 ± 4.676
	2	0.451	2243.2	0.910 ± 0.015	0.589 ± 0.049	41.031 ± 1.126	51.799 ± 4.226	48.600 ± 4.920
	3	0.677	3364.8	0.910 ± 0.015	0.597 ± 0.050	41.222 ± 1.145	50.691 ± 4.207	47.916 ± 4.888
	4	0.902	4486.4	0.914 ± 0.015	0.607 ± 0.048	41.326 ± 1.121	50.346 ± 4.208	47.164 ± 5.143
WideResNet-12	1	0.281	1397.2	0.906 ± 0.015	0.583 ± 0.053	40.929 ± 1.121	52.195 ± 4.247	49.940 ± 4.570
	2	0.562	2794.4	0.909 ± 0.014	0.588 ± 0.051	41.129 ± 1.091	51.283 ± 4.200	48.631 ± 4.712
	3	0.843	4191.7	0.910 ± 0.014	0.593 ± 0.052	41.167 ± 1.156	50.876 ± 4.270	48.018 ± 4.841
	4	1.124	5589.0	0.914 ± 0.015	0.615 ± 0.050	41.379 ± 1.167	49.820 ± 4.245	47.146 ± 5.062
WideResNet-14	1	0.336	1672.9	0.907 ± 0.015	0.586 ± 0.052	41.007 ± 1.122	51.752 ± 4.236	49.457 ± 4.723
	2	0.673	3345.8	0.911 ± 0.015	0.599 ± 0.051	41.193 ± 1.168	50.778 ± 4.248	47.957 ± 4.935
	3	1.009	5018.6	0.913 ± 0.014	0.607 ± 0.050	41.382 ± 1.089	50.055 ± 4.281	47.207 ± 5.012
	4	1.346	6691.5	0.913 ± 0.014	0.610 ± 0.049	41.342 ± 1.069	50.378 ± 4.156	47.262 ± 4.924
WideResNet-16	1	0.392	1948.5	0.909 ± 0.015	0.594 ± 0.051	41.116 ± 1.085	51.414 ± 4.216	48.995 ± 4.740
	2	0.784	3897.0	0.913 ± 0.015	0.605 ± 0.052	41.306 ± 1.168	50.307 ± 4.346	47.399 ± 5.078
	3	1.175	5845.6	0.914 ± 0.014	0.610 ± 0.051	41.431 ± 1.125	49.821 ± 4.229	47.138 ± 4.981
	4	1.567	7794.1	0.913 ± 0.014	0.610 ± 0.049	41.391 ± 1.076	49.965 ± 4.211	47.179 ± 4.962
WideResNet-18	1	0.447	2224.2	0.910 ± 0.015	0.599 ± 0.052	41.089 ± 1.188	51.175 ± 4.312	48.608 ± 4.920
	2	0.894	4448.3	0.912 ± 0.015	0.604 ± 0.051	41.294 ± 1.176	50.244 ± 4.359	47.296 ± 5.078
	3	1.341	6672.5	0.914 ± 0.014	0.616 ± 0.048	41.399 ± 1.153	49.594 ± 4.133	46.743 ± 5.037
	4	1.789	8896.7	0.915 ± 0.014	0.605 ± 0.044	41.368 ± 1.103	50.309 ± 3.865	46.726 ± 5.020

computational cost. Although the same weights are used across all iterations, each iteration still involves a forward pass and solving the optimization equation, which contributes to the overall computational load. Therefore, the computational cost remains significant even with shared weights, as computations are performed for each iteration independently.

2.7.2 | Iteration Specific Denoising

Using unshared weights, the CNN denoiser can learn different filters and features at each iteration. This allows it to adapt to the specific noise characteristics present in different iterations of the reconstruction process. Imagine that the noise may be more prominent in earlier iterations and more subtle in later iterations. The unshared weights allow the denoiser to address these variations effectively.

2.7.3 | Selection of K

The complexity of a model-based deep learning architecture primarily depends on the unrolling parameter because higher unrolling parameters increase the gradient calculation complexity during end-to-end training. Therefore, the selection of the unrolling parameter is a crucial decision that must be made experimentally. In existing model-based deep learning techniques, such as LPCNN and SpiNet-QSM, CNN weights are shared across iterations. Thus, the choosing K parameter is even difficult for the effective utilization of the model-based deep learning architecture. As the number of iterations increases, learning a common regularization term becomes more difficult owing to shared weights. As the number of iterations increases, learning a common regularization term becomes more difficult owing to the shared weights, limiting the ability of the CNN to address the QSM problem effectively. In the proposed ISDU-QSMNet, leveraging unshared weights allows us to use higher unrolling parameters, such as $K = 4$, for QSM solving.

Experiments with K values greater than 4 were initially excluded to mitigate the increased complexity and training difficulties associated with higher values. This is because, we hypothesized that increasing the CNN complexity and the number of unrolling iterations (K) could potentially improve QSM reconstruction. To explore this further, we expanded our analysis by including experiments with a broader range of K values, including those exceeding 4, to assess their effectiveness for larger K settings. Table 4 provides details on key parameters for the proposed ISDU-QSMNet, including the training time per epoch, GPU RAM usage during training with a batch size of 2, model size (which increases with K), and the model's parameter space. Additionally, it presents various performance metrics of the proposed ISDU-QSMNet across different levels of complexity by varying K.

There is no universal strategy for selecting the optimal K value, as it depends on multiple factors such as the dataset, hardware constraints, and the desired trade-off between accuracy and computational efficiency. Therefore, experimentation with different K values is necessary to determine the best configuration for the model, depending on whether the priority is higher accuracy (with larger K) or faster inference (with smaller K). observation.

TABLE 4 | Regularization parameters (λ or λ_i for $i = 1,2,3,4$) and step size (α) values used for different model-based deep learning methods in this study. All configurations reported in this table correspond to models trained using the full training dataset from the SNU dataset [22].

Model	Regularization parameter (λ)	Step size (α)
LPCNN, $K=4$	—	5.6003
SpiNet-QSM, $K=4$	$\lambda=0.0384$	—
MoDL-QSM-SW, $K=4$	$\lambda=0.1565$	—
ISDU-QSMNet-USW, $K=3$	$\lambda_1=0.0444$	—
	$\lambda_2=0.1227$	—
	$\lambda_3=0.2197$	—
ISDU-QSMNet-USW-RS, $K=3$	$\lambda_1=0.0500$	—
	$\lambda_2=0.1196$	—
	$\lambda_3=0.1887$	—
ISDU-QSMNet-USW, $K=4$	$\lambda_1=0.0669$	—
	$\lambda_2=0.0746$	—
	$\lambda_3=0.1664$	—
	$\lambda_4=0.2905$	—
ISDU-QSMNet-USW-RS, $K=4$	$\lambda_1=0.0911$	—
	$\lambda_2=0.0668$	—
	$\lambda_3=0.1531$	—
	$\lambda_4=0.1970$	—

Although no specific algorithm exists for determining the optimal K value, we relied on empirical observations to guide our choice. As the unrolling parameter K increases, the regularization effect becomes stronger in the later iterations, as seen in Table 5, where the regularization parameter λ_i increases with each iteration. The increasing λ_i means that as we move deeper into the unrolling process, the model places more emphasis on the regularization term $\| \chi - D_{Wk}(\chi) \|_2^2$ and less on the fidelity term $\| \phi\chi - y \|_2^2$. In other words, as λ_i increases, the contribution from the denoising regularizer $(\chi - D_{Wk}(\chi))$ becomes more dominant, while the data consistency term becomes less influential. This tradeoff leads to the observation that as K increases and more iterations are added, the contribution from the later iterations to the final output becomes smaller. Beyond a certain K, the additional iterations contribute less to the overall learning, and the benefits of further increasing K become limited.

2.7.4 | Selection of Subset Size (n)

Training model-based deep learning techniques is generally more challenging and time-consuming than training pure deep learning models, especially with higher unrolling parameters. Existing model-based techniques often share weights across

TABLE 5 | Performance metrics and training configurations for ISDU-QSMNet-USW and ISDU-QSMNet-USW-RS at different unrolling iteration values (K), evaluated using the full training dataset from the SNU dataset [22]. Each row reports model complexity (training time per epoch, model size, GPU memory usage, and number of parameters) alongside reconstruction accuracy metrics (SSIM, xSIM, pSNR, NRMSE, and HFEN), presented as mean ± standard deviation.

Method	K	Training time/epoch	Model size (MB)	GPU-RAM (GB)	No. param. (M)	SSIM (±)	xSIM (±)	pSNR (±)	NRMSE (±)	HFEN (±)
ISDU-QSMNet-USW	1	30	1.800	6	0.447	0.910 ± 0.015	0.599 ± 0.052	41.089 ± 1.188	51.175 ± 4.312	48.608 ± 4.920
ISDU-QSMNet-USW	2	60	3.600	9	0.894	0.912 ± 0.015	0.604 ± 0.051	41.294 ± 1.176	50.244 ± 4.359	47.296 ± 5.078
ISDU-QSMNet-USW	3	90	5.500	12	1.348	0.914 ± 0.014	0.616 ± 0.048	41.399 ± 1.153	49.594 ± 4.133	46.743 ± 5.037
ISDU-QSMNet-USW	4	120	7.300	15	1.789	0.915 ± 0.014	0.605 ± 0.044	41.368 ± 1.103	50.309 ± 3.865	46.726 ± 5.020
ISDU-QSMNet-USW	5	150	9.100	18	2.236	0.915 ± 0.014	0.619 ± 0.047	41.494 ± 1.129	49.371 ± 4.083	46.471 ± 5.015
ISDU-QSMNet-USW	6	180	11.000	21	2.683	0.916 ± 0.014	0.621 ± 0.046	41.438 ± 1.102	49.547 ± 4.061	46.455 ± 5.096
ISDU-QSMNet-USW-RS	2	15	3.600	9	0.894	0.914 ± 0.015	0.610 ± 0.050	41.307 ± 1.161	50.381 ± 4.376	47.433 ± 5.178
ISDU-QSMNet-USW-RS	3	30	5.500	12	1.342	0.914 ± 0.014	0.614 ± 0.047	41.368 ± 1.129	49.798 ± 4.146	46.988 ± 5.037
ISDU-QSMNet-USW-RS	4	60	7.300	15	1.789	0.916 ± 0.014	0.618 ± 0.046	41.415 ± 1.131	49.749 ± 4.133	46.562 ± 5.151
ISDU-QSMNet-USW-RS	5	75	9.100	18	2.236	0.914 ± 0.014	0.610 ± 0.045	41.320 ± 1.098	50.052 ± 3.938	46.978 ± 4.924
ISDU-QSMNet-USW-RS	6	90	11.000	21	2.683	0.916 ± 0.013	0.616 ± 0.045	41.530 ± 1.032	49.639 ± 3.929	46.539 ± 4.959

TABLE 6 | Performance metrics and training configurations for ISDU-QSMNet-USW and ISDU-QSMNet-USW-RS (both with $K = 4$) under different subset sampling values (n), evaluated on the SNU dataset using full training data conditions. Metrics include SSIM, xSIM, pSNR, NRMSE, and HFEN, reported as mean ± standard deviation. Training time per epoch is also included to reflect computational efficiency.

Method	n	Training time/epoch	SSIM (±)	xSIM (±)	pSNR (±)	NRMSE (±)	HFEN (±)
ISDU-QSMNet-USW-RS, $K=4$	1000	15	0.912 ± 0.014	0.606 ± 0.048	41.271 ± 1.152	50.282 ± 4.118	47.489 ± 4.904
ISDU-QSMNet-USW-RS, $K=4$	2000	30	0.913 ± 0.014	0.607 ± 0.046	41.230 ± 1.151	50.465 ± 4.092	47.305 ± 4.984
ISDU-QSMNet-USW-RS, $K=4$	3000	45	0.914 ± 0.014	0.614 ± 0.047	41.368 ± 1.129	49.798 ± 4.146	46.988 ± 5.037
ISDU-QSMNet-USW-RS, $K=4$	4000	60	0.916 ± 0.014	0.618 ± 0.046	41.415 ± 1.131	49.749 ± 4.133	46.562 ± 5.151
ISDU-QSMNet-USW-RS, $K=4$	5000	75	0.915 ± 0.014	0.617 ± 0.046	41.454 ± 1.126	49.565 ± 4.058	46.590 ± 5.041
ISDU-QSMNet-USW-RS, $K=4$	6000	90	0.917 ± 0.014	0.615 ± 0.046	41.580 ± 1.154	49.647 ± 4.086	46.464 ± 5.111
ISDU-QSMNet-USW, $K=4$	—	120	0.915 ± 0.014	0.605 ± 0.044	41.368 ± 1.103	50.309 ± 3.865	46.726 ± 5.020

iterations, limiting their ability to use large unrolling parameters owing to constrained weight parameters. However, in the proposed ISDU-QSMNet, the weights are unshared and specific to each denoiser, allowing for larger unrolling parameters but resulting in longer training times. To address this, random subset sampling can be employed, in which each epoch trains the model on a random subset of n samples. This strategy helps reduce training time and it also will not leads to abrupt weight updates due to the physics-informed QSM gradients. In full-data training, a subset size of $n = 4000$ (approximately 25% of the dataset) was used, effectively halving the training time. Additional experiments were conducted with $n = 1000$, 2000, 3000, 4000, 5000, and 6000 to analyze training efficiency and performance trade-offs. Table 6 summarizes the training and performance metrics of ISDU-QSMNet-USW-RS with $K = 4$ across these varying subset sizes. For experiments involving limited training data, subset sampling was not used due to the inherently small dataset size.

2.8 | Experiments

2.8.1 | Effect of Dataset Size

To evaluate the impact of data availability on model performance, the ISDU-QSMNet was evaluated using two experiments: training on complete data and limited data training.

2.8.2 | Training on Complete Data

For this study, the SNU dataset was used, comprising scans from 12 healthy volunteers, each with five different head orientations. From this dataset, 25 scans from five subjects were selected for training, with data augmentation increasing the total number of scans to 75. Additionally, five scans from one subject were set aside for validation and 30 scans from six subjects were used for testing. As part of this study, three model-based deep learning implementations were explored.

1. A model-based deep learning method using a CNN denoiser-based regularizer with shared weights, referred to as **MoDL-QSM-SW**.
2. A model-based deep learning method utilizing a CNN denoiser-based regularizer with unshared weights and iteration-specific training parameters, referred to as **ISDU-QSMNet-USW**.
3. A model-based deep learning method incorporating a CNN denoiser-based regularizer with unshared weights and iteration specific training parameters, combined with random subset sampling during each training epoch to reduce training time, referred to as **ISDU-QSMNet-USW-RS**.

Although ISDU-QSMNet-USW and ISDU-QSMNet-USW-RS share the same architecture, the key difference is the use of random subset sampling in ISDU-QSMNet-USW-RS. The results from the ISDU-QSMNet-USW-RS experiments were treated as the ISDU-QSMNet results for comparison with other models. These three experiments (MoDL-QSM-SW, ISDU-QSMNet-USW, and ISDU-QSMNet-USW-RS) were conducted using identical training settings to properly evaluate the capabilities of each approach. Experiments were conducted with different unrolling iterations ($K = 1, 2, 3, 4$) to develop models of varying complexity. Subsequently, to compare ISDU-QSMNet with other existing model-based deep learning methods, we trained LPCNN and SpiNet-QSM, as well as popular deep learning models, such as QSMnet, DeepQSM, and xQSM. For this full data training experiments, a single-fold validation approach was used. The training was conducted on SNU data from 12 subjects, with each subject having five orientations. In this fold, five orientations from the first five subjects were used for training, one subject (subject 6) was used for validation, and the remaining six

subjects (subjects 7–12) were used for testing. The final results were reported as the average reconstruction performance across all test subjects.

2.8.3 | Training on Limited Data

An experiment was conducted to assess the reconstruction performance of the aforementioned methods using limited training data. For this setup, the training dataset included data from a single subject, supplemented with 15 augmented scans, whereas the validation set remained unchanged from the full data training scenario. The test set consisted of data from 10 additional subjects. This reduced dataset represents approximately 16% of the data used in the full-data training experiment. The same training configurations described earlier were applied to the deep learning models for this limited training-data scenario. Both the limited and full data training experiments were conducted independently, with no knowledge transfer between them. Specifically, the weights obtained from the limited data experiments were not used to initialize the models in the full data experiments, and vice versa. For the limited training data experiments, an inter-subject validation approach was used. Five subjects were selected for training, one subject was reserved for validation, and six subjects were consistently used for testing. This setup resulted in five independent experiments, where each experiment utilized one of the five training subjects for training while keeping the validation subject constant across all experiments. The same six test subjects were used in every experiment to ensure consistency. The results from all five experiments were consolidated to produce overall metrics. Specifically, in one experimental iteration, subjects 1–5 were used for training, the 6th subject was used for validation, and testing was conducted on subjects 7–12. Consequently, in the consolidated results, each subject's test outcomes appeared five times, reflecting their presence in different experimental configurations. The test subjects (subjects 7–12) from the SNU dataset were kept the same across both full and limited training data experiments. This consistency ensures that the evaluation metrics are directly comparable, allowing for a meaningful assessment of performance differences between the two training scenarios.

2.8.4 | Statistical Analysis

A two-tailed paired t test was performed to assess the statistical significance of differences in HFEN between the proposed ISDU-QSMNet and other existing methods, using a significance level of $P = 0.05$. For the full training data experiments, a single-fold evaluation was carried out. In contrast, for the limited training data experiments, the results were derived from the consolidation of five separate experimental runs. Detailed experimental setups can be found in Sections 2.8.2 and 2.8.3.

2.8.5 | Performance on Other Datasets

To assess the robustness and generalization of the model, pretrained models were evaluated on datasets with varying acquisition parameters, vendors, and signal-to-noise ratios (SNR). Specifically, models trained on SNU data under full data training conditions were tested on LPCNN data [39], RC-1 data [41], and RC-2 data [42] datasets. These models were tested on unseen data, in which the preprocessed local field maps were provided directly by the respective authors. No additional preprocessing was performed prior to reconstruction.

2.8.6 | Evaluation on Clinical Data With Nonisotropic Resolution

Although the proposed ISDU-QSMNet was not explicitly designed or trained to be resolution-independent, we evaluated its generalizability across different resolutions using a hemorrhage dataset [44] acquired on a GE 3 T MR scanner. The data has a matrix size of $256 \times 256 \times 66$, voxel size of $0.86 \times 0.86 \times 2\,\text{mm}^3$, and a repetition time (TR) of 42.58 ms. In contrast, the models were trained on the SNU dataset with an isotropic resolution of $1 \times 1 \times 1\,\text{mm}^3$. This evaluation was designed to test model robustness under out-of-distribution conditions, particularly in the presence of hemorrhagic lesions for checking on clinical data.

2.8.7 | ROI Analysis

The local susceptibility values were compared across different reconstruction methods to assess the clinical applicability of the proposed ISDU-QSMNet. For this analysis, regions of interest (ROIs) were defined across the full volume of the brain, including the caudate nucleus (CN), putamen (PUT), globus pallidus (GP), white matter (left and right white matter), and gray matter (left and right gray matter). These ROIs were segmented using ITKsnap [46] and SynthSeg [47] for six test subjects from the SNU dataset. To evaluate the model's performance, reconstructions from models trained on SNU datasets from both the full and limited training were utilized.

2.8.8 | Ablation Study

To evaluate the contributions of individual components in ISDU-QSMNet, ablation studies were performed focusing on two key aspects: (i) unshared weights and (ii) random subset sampling. All experiments were conducted using the full training data with an unrolling parameter of $K = 4$, under consistent training and implementation settings.

2.8.9 | Unshared Weights

To assess the impact of unshared weights, a comparison was made with models employing shared weights, where a single CNN denoiser was reused across all iterations instead of using iteration-specific denoisers. Ablation experiments 1 and 2 were conducted to analyze the effects of unshared weights.

2.8.10 | Unshared Weights and Random Subset Sampling

The combined effect of unshared weights and random subset sampling was analyzed through three experimental setups:

(Experiment 1) shared weights without random subset sampling (Experiment 2) shared weights with random subset sampling, and (Experiment 3) unshared weights without random subset sampling.

3 | Results

3.1 | Effect of Dataset Size

3.1.1 | Training on Complete Data

The quantitative performance metrics such as structural similarity index measure (SSIM), peak signal-to-noise ratio (pSNR), normalized mean square error (NRMSE), and high-frequency error norm (HFEN) [41] with respect to COSMOS for the different QSM reconstruction methods considered in this study are summarized in Table 7. Additionally, the reconstructions from all model-based experiments conducted across different unrolling iterations ($K = 1, 2, 3, 4$), using various configurations such as shared or unshared weights and either full-set or random subset sampling, are summarized in Table 8, with sample image reconstructions from each method displayed shown in Figure 3. To better illustrate alignment with the gold standard COSMOS, a representative reconstruction from each method is shown in Figure 4a. Additionally, QSM reconstruction images for subjects 7, 8, and 9 from the SNU test dataset, including axial, coronal, and sagittal views, have been provided in Figures 3–5 of the supplementary material. Table 9 describes the training time and inference time. The proposed ISDU-QSMNet demonstrated statistically significant improvements over existing model-based deep-learning approaches, outperforming SpiNet-QSM ($P = 0.01$) and LPCNN ($P = 6.98 \times 10^{-5}$). It also outperformed the existing deep learning methods, including QSMNet ($P = 1.10 \times 10^{-3}$), DeepQSM ($P = 9.5 \times 10^{-6}$), and xQSM ($P = 3.80 \times 10^{-4}$). For a fair comparison, ISDU-QSMNet was evaluated under training conditions similar to SpiNet-QSM and LPCNN. Additionally, SpiNet-QSM performance matched the performance of model-based deep learning with shared weights (MoDL-QSM-WS) with $P = 0.87$ and achieved better reconstruction results than LPCNN ($P = 1.27 \times 10^{-07}$).

3.1.2 | Training on Limited Data

Table 10 summarizes the quantitative performance metrics of various QSM reconstruction methods evaluated under limited data conditions. The results indicate that as the training data were reduced, the quality of the reconstructed susceptibility maps decreased compared to those obtained using the full dataset. An example of reconstruction is shown in Figure 4b. Figure 5 presents scatter plots of the quantitative performance of the proposed method and other approaches for both complete and limited training data, showing that ISDU-QSMNet reconstruction closely matches the gold-standard COSMOS map. The results showed that ISDU-QSMNet performed similarly to the model-based deep-learning approach with shared weights (MoDL-QSM-WS) ($P = 0.603$) and SpiNet-QSM ($P = 0.845$). However, ISDU-QSMNet achieved significantly better reconstruction results than the LPCNN ($P = 7.72 \times 10^{-7}$). ISDU-QSMNet also showed statistically significant improvements over existing deep learning approaches, including QSMnet ($P = 1.16 \times 10^{-21}$), DeepQSM ($P = 6.23 \times 10^{-25}$), and xQSM ($P = 7.30 \times 10^{-25}$). Another observation from our experiments was that SpiNet-QSM outperformed the LPCNN ($P = 1.27 \times 10^{-7}$). Both SpiNet and LPCNN showed better performance than the deep learning methods QSMnet, DeepQSM, and xQSM. To ensure a fair comparison, ISDU-QSMNet was evaluated along with SpiNet-QSM and LPCNN under similar training conditions.

TABLE 7 | Quantitative performance metrics (SSIM, xSIM, pSNR, NRMSE, and HFEN) for various QSM reconstruction methods, evaluated on the SNU dataset using models trained on the full training data from the same dataset. The results, obtained through single-fold cross-validation, highlight the best performance for each metric in bold.

	METRICS				
Method	**SSIM**	**xSIM**	**pSNR**	**NRMSE**	**HFEN**
QSMnet	0.907 ± 0.029	0.600 ± 0.047	40.411 ± 1.230	53.543 ± 4.948	52.880 ± 9.587
DeepQSM	0.904 ± 0.029	0.589 ± 0.046	40.343 ± 1.188	54.061 ± 4.818	54.110 ± 9.277
xQSM	0.906 ± 0.018	0.600 ± 0.048	40.342 ± 1.246	54.075 ± 5.058	52.397 ± 0.259
LP-CNN, $K = 4$	0.905 ± 0.014	0.572 ± 0.051	40.345 ± 1.303	56.108 ± 5.039	53.701 ± 5.630
SpiNet-QSM, $K = 4$	0.912 ± 0.015	0.591 ± 0.059	40.470 ± 1.343	53.531 ± 5.586	50.559 ± 6.359
NDI	0.868 ± 0.035	0.487 ± 0.090	38.257 ± 1.351	70.089 ± 8.228	66.152 ± 8.631
FANSI	0.870 ± 0.024	0.413 ± 0.077	38.584 ± 1.398	67.239 ± 7.993	63.152 ± 8.636
MoDL-QSM-SW, $K = 4$	0.912 ± 0.015	0.601 ± 0.051	40.560 ± 1.393	53.406 ± 5.300	50.467 ± 6.020
ISDU-QSMNet-USW, $K = 4$	0.915 ± 0.014	0.610 ± 0.043	40.868 ± 1.459	52.308 ± 5.865	49.725 ± 6.619
ISDU-QSMNet-USW-RS, $K = 4$	**0.916 ± 0.014**	**0.617 ± 0.056**	**40.914 ± 1.495**	**52.033 ± 5.704**	**49.310 ± 6.608**

TABLE 8 | Performance metrics (SSIM, xSIM, pSNR, NRMSE, and HFEN) for various model-based deep learning implementations in QSM reconstruction, trained on the SNU dataset [22]. The results are assessed under both full and limited training data conditions, with different unrolling parameters (K). Each metric is reported as mean ± standard deviation. All results correspond to a single-fold evaluation.

Experiment	Method	Unrolling parameter (K)	SSIM	xSIM	pSNR	NRMSE	HFEN
Full training data	**MoDL-QSM-SW**	**1**	0.909 ± 0.014	0.599 ± 0.051	41.089 ± 1.187	51.174 ± 4.312	48.608 ± 4.920
		2	0.907 ± 0.014	0.578 ± 0.053	41.030 ± 1.136	51.576 ± 4.221	48.948 ± 4.687
		3	0.910 ± 0.015	0.590 ± 0.053	41.093 ± 1.180	51.273 ± 4.370	47.869 ± 5.006
		4	0.911 ± 0.015	0.604 ± 0.052	41.221 ± 1.739	50.606 ± 4.371	47.767 ± 5.007
	ISDU-QSMNet-USW	1	0.909 ± 0.014	0.599 ± 0.051	41.089 ± 1.187	51.174 ± 4.312	48.608 ± 4.920
		2	0.912 ± 0.014	0.604 ± 0.051	41.293 ± 1.176	50.243 ± 4.358	47.295 ± 5.078
		3	0.914 ± 0.014	0.615 ± 0.047	41.398 ± 1.152	49.594 ± 4.132	46.743 ± 5.036
		4	0.915 ± 0.014	0.604 ± 0.043	41.367 ± 1.102	50.308 ± 3.865	46.725 ± 5.019
	ISDU-QSMNet-USW-RS	1	0.909 ± 0.014	0.599 ± 0.051	41.089 ± 1.187	51.174 ± 4.312	48.608 ± 4.920
		2	0.913 ± 0.014	0.609 ± 0.050	41.307 ± 1.161	50.381 ± 4.376	47.433 ± 5.177
		3	0.914 ± 0.014	0.614 ± 0.046	41.368 ± 1.128	49.797 ± 4.145	46.987 ± 5.036
		4	0.916 ± 0.014	0.618 ± 0.046	41.415 ± 1.130	49.749 ± 4.133	46.562 ± 5.151
Limited training data	**MoDL-QSM-SW**	1	0.893 ± 0.028	0.532 ± 0.084	39.839 ± 1.504	57.484 ± 7.602	55.401 ± 8.924
		2	0.892 ± 0.027	0.525 ± 0.081	39.820 ± 1.446	57.396 ± 7.304	55.378 ± 8.639
		3	0.895 ± 0.028	0.537 ± 0.084	39.917 ± 1.492	57.175 ± 7.599	54.878 ± 9.045
		4	0.893 ± 0.028	0.528 ± 0.082	39.888 ± 1.479	57.336 ± 7.457	55.184 ± 8.931
	ISDU-QSMNet-USW	1	0.893 ± 0.028	0.532 ± 0.084	39.839 ± 1.504	57.484 ± 7.602	55.401 ± 8.924
		2	0.895 ± 0.028	0.541 ± 0.084	39.925 ± 1.505	57.124 ± 7.569	54.814 ± 9.094
		3	0.895 ± 0.025	0.538 ± 0.073	39.918 ± 1.389	57.205 ± 6.567	55.032 ± 7.878
		4	0.896 ± 0.029	0.545 ± 0.087	39.966 ± 1.523	56.679 ± 7.711	54.507 ± 9.334

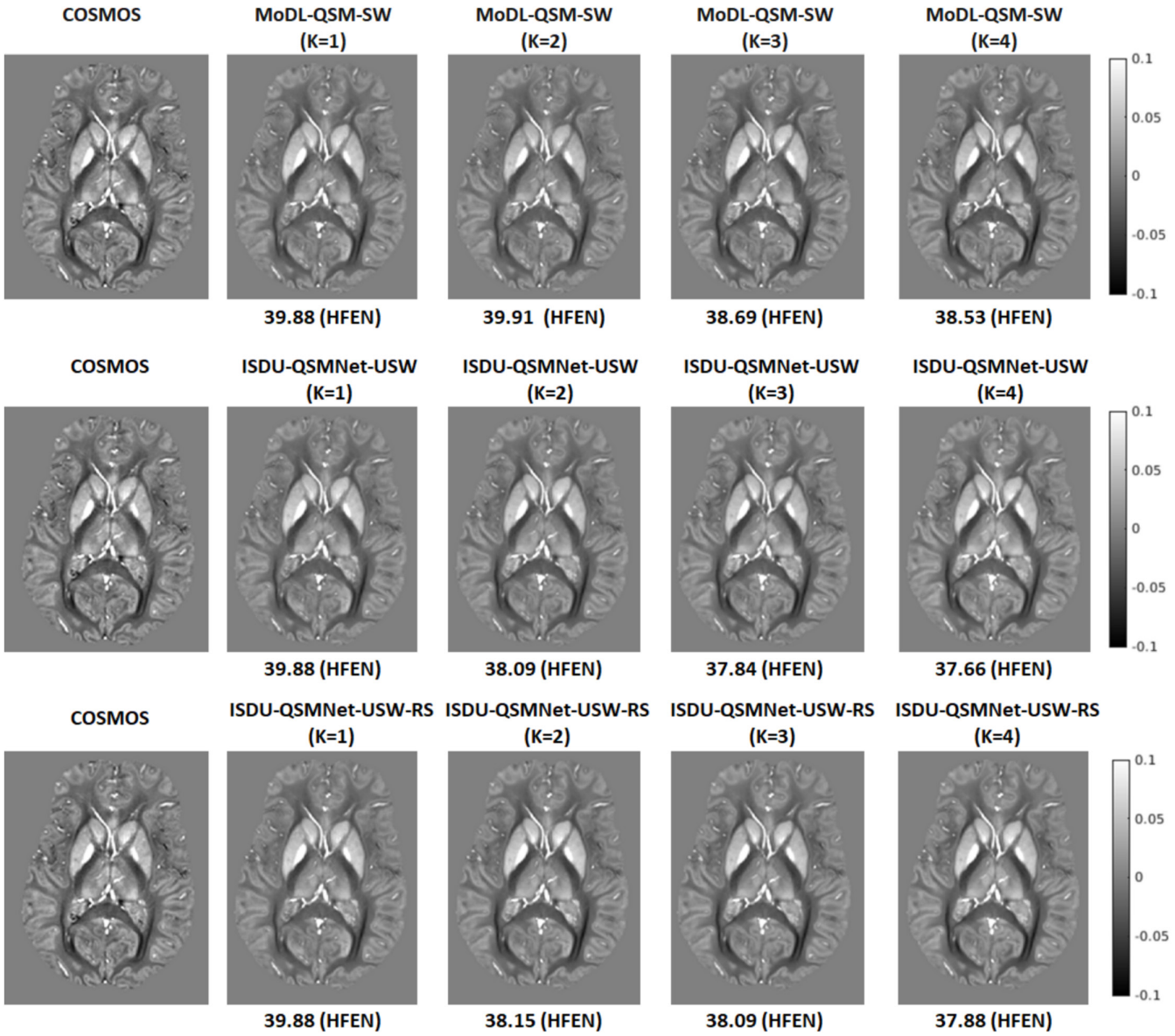

FIGURE 3 | Example susceptibility reconstructions from subject 7 of the SNU dataset, obtained using models trained on the full training data. The comparison includes MoDL-QSM with a shared-weights denoiser, ISDU-QSMNet with unshared weights per iteration, and ISDU-QSMNet with both unshared weights and random subset sampling. Reconstructions are shown for different unrolling parameters ($K = 1, 2, 3, 4$), highlighting the effect of iterative depth on reconstruction quality.

3.2 | Performance on Other Datasets

Table 11 presents the quantitative performance metrics for the various QSM reconstruction methods tested on the LPCNN, RC-1, and RC-2 datasets. ISDU-QSMNet consistently outperformed the other methods on these datasets. For the LPCNN data, ISDU-QSMNet (with random sampling) achieved the best results compared to the model-based deep learning methods (LPCNN and SpiNet-QSM), and completely outperformed the pure deep learning methods (QSMnet, DeepQSM, and xQSM), as evidenced by the lower HFEN and NRMSE. On the RC-1 data, ISDU-QSMNet demonstrated better results than SpiNet-QSM and LPCNN and surpassed the deep learning methods QSMnet, DeepQSM, and xQSM. The deep-learning methods matched the performance of the LPCNN. On both LPCNN data and RC-1 data, model-based and pure deep learning methods achieved better performance than the iterative methods of NDI and FANSI. Visual comparisons of reconstructed susceptibility maps from various QSM methods, shown in axial, coronal, and sagittal views, are provided in Figures 1 and 2 of the supplementary material for the RC-1 and LPCNN datasets respectively. On the RC-2 dataset, the iterative method FANSI demonstrated the highest performance among the evaluated approaches, as reported in [43]. Model-based deep learning methods performed slightly better than NDI, with the proposed ISDU-QSMNet showing a modest advantage over LPCNN and SpiNet-QSM. In comparison, purely data-driven deep learning methods yielded lower performance than NDI, SpiNet-QSM, and LPCNN. The improved performance on RC-2 is mainly due to the use of data-adaptive regularization parameters, which help mitigate the effects of noise present in the dataset. The slight improvements observed in model-based approaches can be attributed to the incorporation of underlying physics into the learning process. Overall, model-based

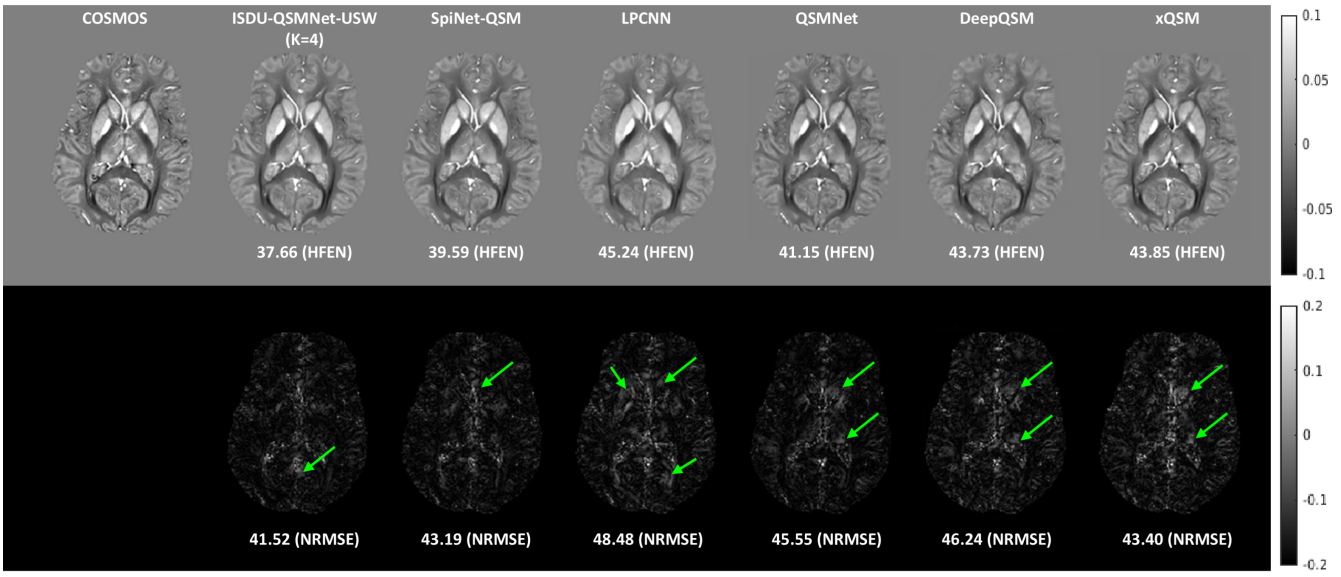

(a)

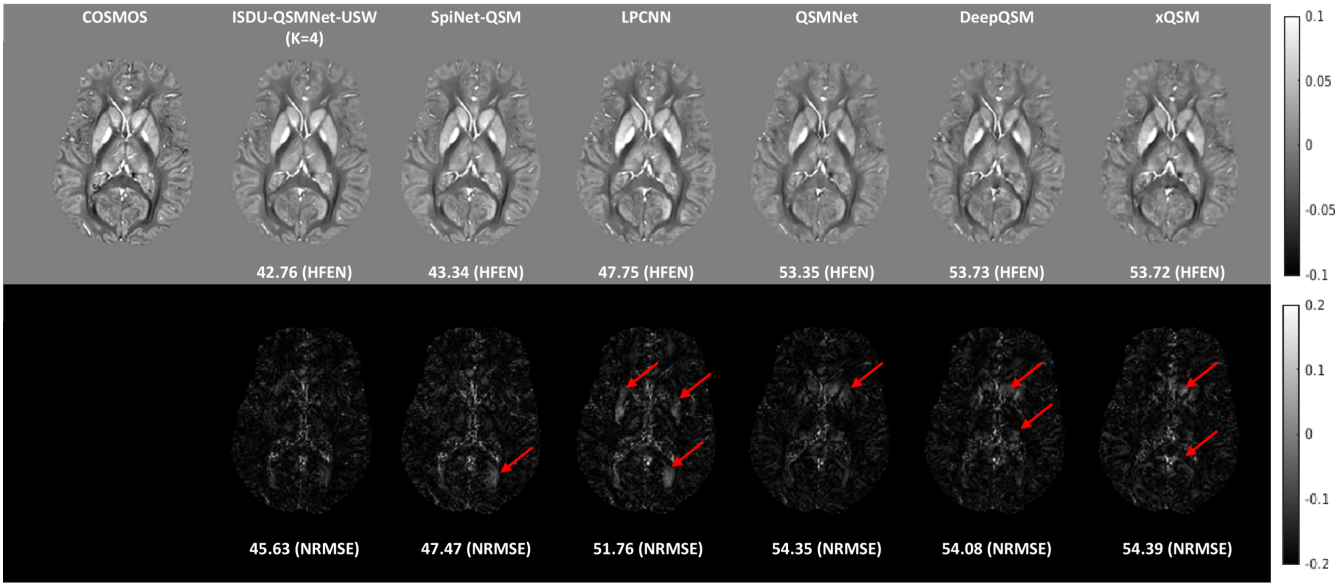

(b)

FIGURE 4 | (a) The first row shows susceptibility map reconstructions for subject 7 from the SNU dataset [22], obtained using models trained on the full training dataset. The second row displays the corresponding difference maps with respect to COSMOS. (b) The same subject is reconstructed using models trained with limited training data (16% of the data used in (a)), with difference maps shown in the second row. High-frequency error norm and normalized root mean squared error values are reported below each susceptibility and difference map.

deep-learning methods outperformed pure deep-learning methods with ISDU-QSMNet, showing the best performance across all datasets.

3.3 | Evaluation on Clinical Data With Anisotropic Resolution

The sample QSM reconstructions for anisotropic resolution are presented in Figure 6. Because ground truth is unavailable for this dataset, we computed the model loss as the l_2 norm of the difference between the input local field and the local field calculated from the reconstructed susceptibility map produced by the trained models, which is obtained by convolving the reconstructed susceptibility map with the dipole kernel (forward model).

3.4 | ROI Analysis

The results of the ROI analysis for models trained on the full dataset are presented in Table 12. This table summarizes the local susceptibility values (mean and standard deviation) of the ROIs for the six subjects, alongside the corresponding COSMOS values for comparison. The findings indicate that the local measurements obtained from the proposed ISDU-QSMNet consistently align with the COSMOS susceptibility measurements. Additionally, Table 12 presents the correlation between the

ISDU-QSMNet results and the COSMOS susceptibility measurements for each region of interest. The results for models trained on the limited dataset are provided in Table 1 of the supplementary material.

3.5 | Ablation Study

Table 13 highlights the significance of each module and demonstrates its impact on the performance metrics.

3.5.1 | Unshared Weights

The absence of unshared weights resulted in a noticeable performance decline, particularly in the HFEN and SSIM metrics, when compared to COSMOS. This performance drop can be attributed to the reduced denoising ability of the models trained with shared weights, which limits their effectiveness in QSM reconstruction. However, when comparing experiments involving shared weights with random subset sampling, the performance was significantly lower than that of the models trained with unshared weights and random subset sampling. This decline is attributed to the reduced denoising capacity of the models with shared weights, which compromises their ability to perform effective QSM reconstruction.

TABLE 9 | Summary of training and inference times for various models trained on the SNU dataset using the full training data setting. The table reports the average training time per epoch (in minutes) and the average inference time per subject (in seconds).

Experiment	Training time (min/epoch)	Inference time (s)
ISDU-QSMNet, $K=4$	120	4.65
SpiNet-QSM, $K=4$	120	4.65
LP-CNN, $K=3$	120	0.33
QSMNet	45	1.65
Deep QSM	30	0.25
xQSM	50	0.96

3.5.2 | Unshared Weights and Random Subset Sampling

In Experiment 3, which utilized unshared weights without random subset sampling, the performance remained consistent and did not show any significant difference compared with Experiment 4, where both unshared weights and random subset sampling were employed. Similarly, in Experiment 1, where shared weights were used without random subset sampling, the performance remained unchanged when compared to Experiment 2, where random subset sampling was applied with shared weights. Although random subset sampling did not significantly impact the performance in these experiments, it offered the advantage of reduced training time. This reduction in training time occurred because the model-based deep learning approach, when combined with random subset sampling, could effectively explore the full dataset when trained for a sufficient number of epochs.

4 | Discussion

This study introduced ISDU-QSMNet, a novel model-based deep learning approach for QSM reconstruction that utilizes an unrolling iterative structure with an iteration-specific CNN denoiser-based trainable regularizer featuring unique denoiser weights for each iteration. When addressing large and complex problems, sufficient training data are typically required to capture all the variations within the data. That is particularly evident in the performance of deep learning methods. Alternatively, incorporating the underlying physics

TABLE 10 | Quantitative performance metrics (SSIM, xSIM, pSNR, NRMSE, and HFEN) for various QSM reconstruction methods, evaluated on the SNU dataset using models trained on limited training data from the same dataset. Results are averaged over five independent experiments, each trained using a single subject from the training set. The best-performing value for each metric is highlighted in bold. Because NDI and FANSI are iterative methods, their results remain consistent and are reported in the same manner as in the full-data training experiments (see Table 7).

	METRICS				
Method	**SSIM**	**xSIM**	**pSNR**	**NRMSE**	**HFEN**
QSMNet	0.866 ± 0.040	0.436 ± 0.127	39.345 ± 1.549	63.164 ± 9.265	63.299 ± 12.285
DeepQSM	0.866 ± 0.040	0.434 ± 0.124	39.355 ± 1.493	63.208 ± 8.792	64.004 ± 11.628
xQSM	0.859 ± 0.054	0.419 ± 0.152	39.230 ± 1.632	64.602 ± 10.161	64.625 ± 12.841
NDI	0.868 ± 0.035	0.487 ± 0.090	38.257 ± 1.351	70.089 ± 8.228	66.152 ± 8.631
FANSI	0.870 ± 0.024	0.413 ± 0.077	38.584 ± 1.398	67.239 ± 7.993	63.152 ± 8.636
LPCNN, $K=4$	0.891 ± 0.019	0.514 ± 0.061	40.179 ± 1.080	57.193 ± 4.167	54.784 ± 4.886
SpiNet-QSM, $K=4$	0.903 ± 0.017	0.560 ± 0.054	40.692 ± 1.137	54.181 ± 4.152	51.474 ± 4.777
MoDL-QSM-SW, $K=4$	0.902 ± 0.017	0.555 ± 0.053	40.635 ± 1.141	54.430 ± 4.128	51.720 ± 4.726
ISDU-QSMNet-USW, $K=4$	0.903 ± 0.019	0.568 ± 0.060	40.714 ± 1.204	53.716 ± 4.371	51.095 ± 5.249

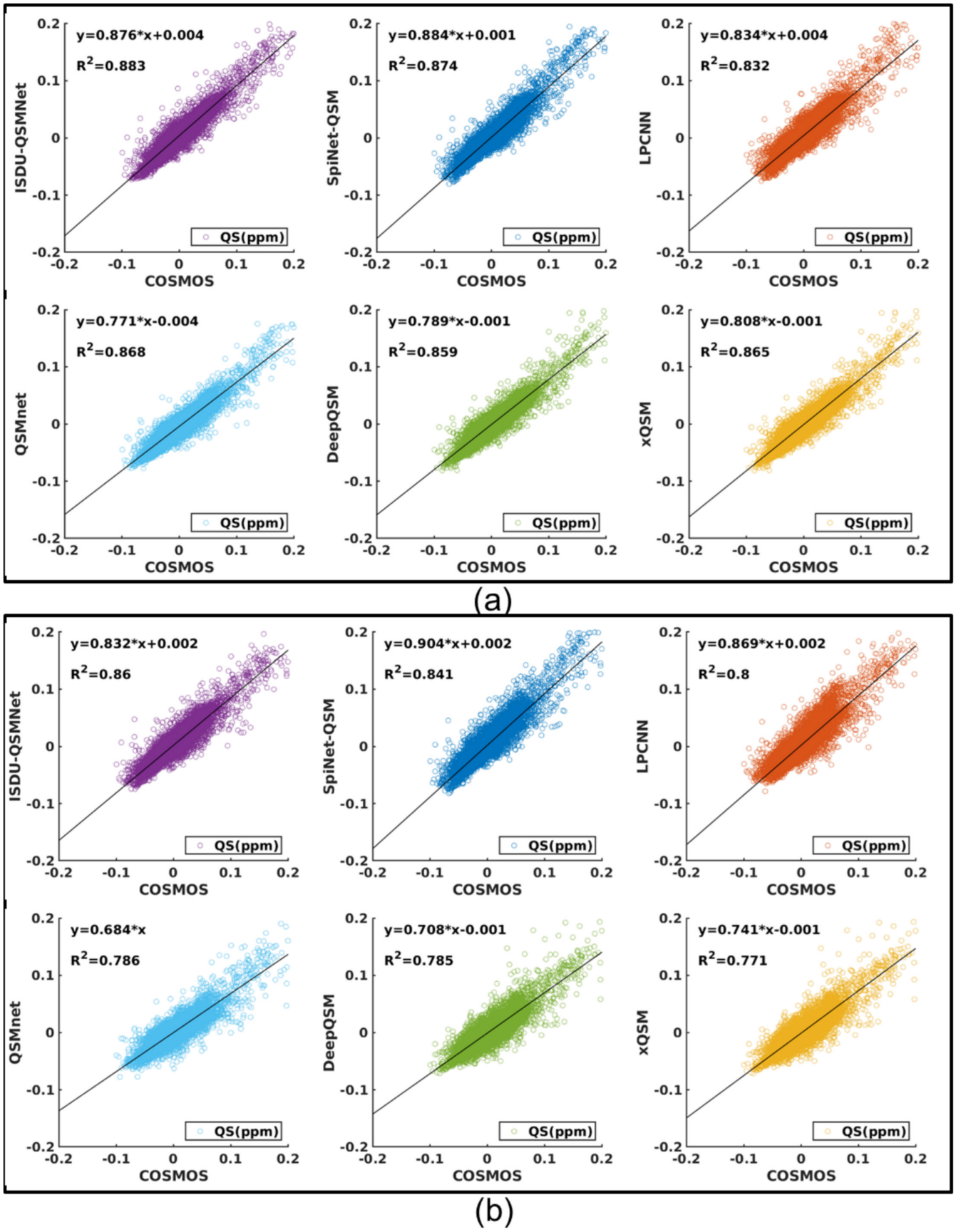

FIGURE 5 | Scatter plots of QSM reconstructions for subject 7 from the SNU dataset [22]. (a) Models trained on the full training dataset. (b) Models trained on the limited training dataset. Each plot compares the reconstructed susceptibility values (QS, in ppm) against the COSMOS reference. In both cases, all voxels within the brain volume were included.

TABLE 11 | Performance metrics (SSIM, xSIM, pSNR, NRMSE, and HFEN) for various QSM reconstruction methods trained on the SNU dataset using models with full training data, evaluated on LPCNN, RC-1, and RC-2 datasets. Results are reported as mean ± standard deviation, with the best performance for each metric highlighted in bold.

		METRICS				
Experiment	**Method**	**SSIM**	**xSIM**	**pSNR**	**NRMSE**	**HFEN**
LPCNN data	QSMnet	0.928 ± 0.015	0.472 ± 0.040	32.987 ± 1.730	61.873 ± 3.377	56.496 ± 4.539
	DeepQSM	0.926 ± 0.015	0.459 ± 0.038	32.998 ± 1.734	61.960 ± 3.086	57.453 ± 4.054
	xQSM	0.924 ± 0.015	0.457 ± 0.039	32.909 ± 1.633	62.938 ± 3.141	58.757 ± 4.384
	LP-CNN	0.916 ± 0.010	0.389 ± 0.202	34.559 ± 1.551	60.607 ± 2.286	55.768 ± 2.850
	SpiNet-QSM	0.931 ± 0.014	0.514 ± 0.051	33.129 ± 1.796	57.499 ± 4.421	54.625 ± 4.800
	MoDL-QSM-SW, $K = 4$	0.931 ± 0.013	0.521 ± 0.049	33.100 ± 1.767	57.246 ± 4.303	54.392 ± 4.685
	ISDU-QSMNet-USW, $K = 4$	0.932 ± 0.013	0.526 ± 0.049	33.094 ± 1.680	56.185 ± 4.512	53.599 ± 4.560
	ISDU-QSMNet-USW-RS, $K = 4$	**0.933 ± 0.013**	**0.535 ± 0.049**	**33.130 ± 1.730**	**56.053 ± 4.584**	**53.577 ± 4.755**
RC-1 data	QSMnet	0.909	0.587	39.764	51.545	49.225
	DeepQSM	0.908	0.574	39.601	52.076	50.175
	xQSM	0.909	0.578	39.560	52.577	50.133
	NDI	0.853	0.512	37.457	61.715	60.728
	FANSI	0.856	0.411	37.970	61.920	59.480
	LP-CNN	0.900	0.557	39.492	52.217	49.970
	SpiNet-QSM	0.916	0.643	40.653	47.150	46.0752
	MoDL-QSM-SW, $K = 4$	0.916	0.627	40.368	47.002	45.041
	ISDU-QSMNet-USW, $K = 4$	0.919	0.635	40.471	46.448	44.710
	ISDU-QSMNet-USW-RS, $K = 4$	**0.919**	**0.641**	**40.556**	**46.082**	**44.651**
RC-2 data (Sim2Snr1)	QSMnet	0.987	0.471	49.318	66.525	58.186
	DeepQSM	0.987	0.445	49.477	67.731	60.366
	xQSM	0.987	0.465	49.168	67.459	59.363
	NDI	0.984	0.596	51.056	55.384	48.661
	FANSI	**0.995**	**0.786**	**55.527**	**32.816**	**22.250**
	LP-CNN	0.991	0.593	51.057	56.424	51.695
	SpiNet-QSM	0.991	0.618	51.336	54.187	50.076
	MoDL-QSM-SW, $K = 4$	0.991	0.654	51.861	51.261	49.186
	ISDU-QSMNet-USW, $K = 4$	0.992	0.671	52.078	49.418	46.250
	ISDU-QSMNet-USW-RS, $K = 4$	0.992	0.676	52.038	49.607	46.100

(Continues)

TABLE 11 | (Continued)

Experiment	Method	METRICS				
		SSIM	xSIM	pSNR	NRMSE	HFEN
RC-2 data (Sim2Snr2)	QSMnet	0.987	0.480	49.305	65.882	57.436
	DeepQSM	0.987	0.452	49.293	67.301	59.893
	xQSM	0.987	0.471	49.130	67.052	58.892
	NDI	0.987	0.636	51.385	52.560	48.063
	FANSI	**0.995**	**0.834**	**56.518**	**29.177**	**20.043**
	LP-CNN	0.991	0.605	50.968	55.377	50.816
	SpiNet-QSM	0.991	0.635	51.300	53.073	49.253
	MoDL-QSM-SW, $K=4$	0.991	0.669	51.604	50.251	48.274
	ISDU-QSMNet-USW, $K=4$	0.992	0.687	51.970	48.199	45.594
	ISDU-QSMNet-USW-RS, $K=4$	0.992	0.689	51.936	48.596	45.282

of the problem drawn from traditional iterative methods into the deep learning framework can substantially enhance model performance, especially in limited-data scenarios, leading to model-based deep learning solutions that are more reliable and consistent than purely data-driven approaches. Conversely, when sufficient training data are available, model-based deep learning approaches may not necessarily outperform pure deep learning models. Among these two paradigms, it remains uncertain which will perform better when evaluated on the same type of data. To address this, more powerful models are needed that can fully leverage the available data and the underlying physics of the problem. When sufficient training data are available and combined with the underlying physics of the problem, it becomes possible to develop robust model-based deep learning approaches that effectively capture data variability. This is especially crucial for QSM, given its inherent complexity and the ill-posed nature of the inverse problem. Because, QSM reconstruction involves handling 3D volumes and requires significant computational resources and well-designed models to manage the intricacies involved. The challenge of ill-posedness must also be addressed in model design. Therefore, an efficient and scalable design is essential for developing a powerful model-based deep learning solution for QSM. The proposed ISDU-QSMNet is specifically designed to address these challenges through a framework that can leverage larger training datasets—something that many existing deep learning and model-based methods struggle to achieve.

First unique challenge addressed by ISDU-QSMNet: Its architecture, based on iteration-specific denoisers with unshared weights, enables the model to better utilize larger training datasets. This capability is lacking in many existing model-based deep learning methods [39, 40].

Second unique challenge addressed by ISDU-QSMNet: Its ability to consistently outperform existing deep learning methods in limited training data scenarios, owing to its physics-informed model-based design that ensures more reliable and stable reconstructions.

Third unique challenge addressed by ISDU-QSMNet: Its strong ability to generalize to unseen conditions, even when the test data are acquired using different parameters, highlights its robustness in real-world clinical scenarios.

4.1 | Mitigating Instability in Subset Sampling

In model-based deep learning, the physics of the QSM model is incorporated into the model formulation, helping to reduce the abrupt weight updates (guided weight updates) that often occur in purely data-driven models when training with subset sampling. This integration also reduces the likelihood of the model getting stuck in the local minima, leading to more stable weight updates.

4.2 | Architectural and Methodological Difference

ISDU-QSMNet builds on the model-based deep learning paradigm through iterative unrolling, a strategy also employed by LP-CNN and SpiNet-QSM. However, several critical architectural distinctions set ISDU-QSMNet apart. First, while all three methods utilize CNN-based regularization, their implementations differ: ISDU-QSMNet and SpiNet-QSM both use CNN denoisers integrated as regularization terms, whereas LP-CNN uses a CNN as a learned proximal operator. Unlike SpiNet-QSM and LP-CNN, which use shared weights across iterations, ISDU-QSMNet employs unshared, iteration-specific denoisers, enabling each stage to learn context-specific refinements. This design offers greater adaptability to varying noise levels and reconstruction errors over the course of unrolling, which is limited in both LP-CNN and SpiNet-QSM due to weight sharing. Second, for solving the data consistency subproblem, ISDU-QSMNet and SpiNet-QSM both use conjugate gradient descent, which ensures efficient and stable convergence. LP-CNN, on the

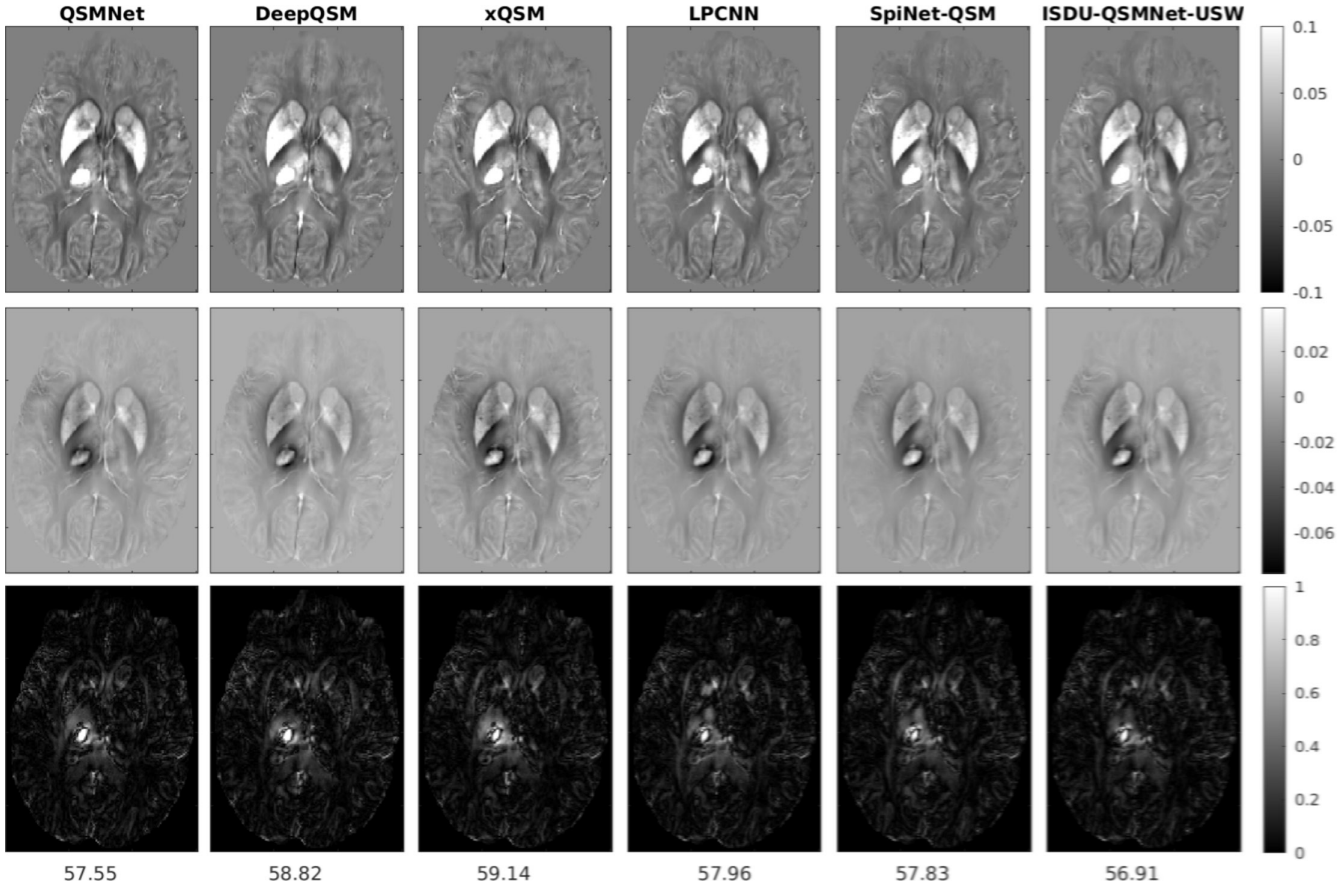

FIGURE 6 | Comparison of QSM reconstructions and estimated local fields (forward model results from reconstruction) and error maps of a hemorrhage data [44]. Top row: Susceptibility maps from different methods. Middle row: Estimated local fields obtained by applying the forward model to each reconstruction. Bottom row: Absolute error maps between forward-estimated and measured local fields (Model loss is shown below the absolute error maps for each method). All images correspond to the same axial slice with consistent intensity ranges.

other hand, employs proximal gradient descent, which is generally less efficient and may converge more slowly.

4.3 | Rethinking Unrolling Efficiency: Moving Beyond Uniform Iterations

Although the proposed ISDU-QSMNet, LP-CNN, and SpiNet-QSM all adopt model-based deep learning strategies, none of these methods explicitly optimize iteration-specific computational complexity. In the iterative unrolling frameworks of QSM, the level of refinement introduced by each iteration tends to diminish with each successive iteration—as illustrated by the trend in regularization parameters in Figure 2 and Table 4. For LP-CNN and SpiNet-QSM, optimizing per-iteration complexity is inherently not in scope due to the use of shared CNN weights across all iterations. Although ISDU-QSMNet introduces iteration-specific denoisers (unlike SpiNet-QSM and LP-CNN, which share weights across iterations), it still uses denoisers of uniform computational complexity at every stage. This overlooks the potential to reduce computational burden in later iterations, where less refinement may be sufficient. A promising future direction would involve designing denoisers with decreasing complexity across iterations—for example, by using shallower networks in later stages—to enhance computational efficiency without degrading reconstruction quality (e.g., the depth of the network can decrease from the i^{th} unrolling to the $(i+1)^{\text{th}}$ unrolling). This is especially relevant given that QSM is a computationally demanding 3D reconstruction task, and optimizing the architecture for efficiency remains an important opportunity for further improvement.

4.4 | Scope and Boundaries of Generalization

Even though ISDU-QSMNet is a model-based deep learning architecture that leverages physical consistency through data fidelity terms, it does not explicitly address resolution or orientation invariance. Although model-based methods are often believed to exhibit improved generalizability, the current architecture was not specifically designed to handle anisotropic resolution or varying dipole orientations. Because the model uses frozen weights trained on the SNU dataset, its parameters are inherently aligned with the characteristics of that dataset, such as isotropic resolution. However, when evaluated on out-of-distribution data, such as anisotropic resolution, the model's generalization primarily relies on the data consistency term, with limited support from the learned priors. Consequently, the model's performance cannot be guaranteed under significantly different testing conditions.

TABLE 12 | Quantitative comparison of susceptibility values (in ppm) and Pearson correlation coefficients with COSMOS across multiple brain ROIs—caudate, putamen, globus pallidus, left and right white matter, and left and right gray matter—evaluated on six test subjects from the SNU dataset. Each method was trained with full training data from SNU dataset. For each subject's ROI, the best-performing method (i.e., susceptibility value with the smallest deviation from COSMOS and highest correlation coefficient) is highlighted in bold.

	Susceptibility values						Correlation with COSMOS					
Method	**Sub-1**	**Sub-2**	**Sub-3**	**Sub-4**	**Sub-5**	**Sub-6**	**Sub-1**	**Sub-2**	**Sub-3**	**Sub-4**	**Sub-5**	**Sub-6**
ROI: Caudate												
COSMOS	0.040 ± 0.027	0.036 ± 0.033	0.036 ± 0.022	0.037 ± 0.024	0.052 ± 0.033	0.044 ± 0.022	1	1	1	1	1	1
QSMnet	0.027 ± 0.022	0.028 ± 0.026	0.031 ± 0.021	0.029 ± 0.021	0.038 ± 0.025	0.035 ± 0.019	0.925	0.889	0.871	0.843	0.915	0.904
DeepQSM	0.031 ± 0.022	**0.034 ± 0.024**	0.033 ± 0.020	0.033 ± 0.021	0.045 ± 0.024	0.036 ± 0.020	0.916	0.873	0.845	0.874	0.908	0.891
xQSM	0.032 ± 0.022	0.030 ± 0.025	0.034 ± 0.021	0.033 ± 0.021	0.047 ± 0.026	0.038 ± 0.021	0.911	0.875	0.870	0.858	0.927	0.905
LP-CNN	0.048 ± 0.021	0.046 ± 0.023	0.044 ± 0.021	0.043 ± 0.021	0.076 ± 0.027	0.060 ± 0.019	0.894	0.810	0.795	0.839	0.858	0.845
SpiNet-QSM	0.047 ± 0.023	**0.038 ± 0.026**	0.038 ± 0.021	**0.037 ± 0.021**	0.058 ± 0.029	0.049 ± 0.020	0.936	0.893	0.879	0.912	0.937	0.939
STAR-QSM	0.023 ± 0.027	0.031 ± 0.034	**0.035 ± 0.028**	0.040 ± 0.028	**0.051 ± 0.035**	0.035 ± 0.024	0.864	0.849	0.816	0.864	0.851	0.859
NDI	0.034 ± 0.022	0.024 ± 0.026	0.028 ± 0.021	0.026 ± 0.019	0.037 ± 0.024	**0.040 ± 0.020**	0.881	0.846	0.812	0.837	0.834	0.848
MoDL-QSM-SW, $K=4$	0.047 ± 0.024	0.040 ± 0.026	0.042 ± 0.022	0.038 ± 0.022	0.062 ± 0.031	0.049 ± 0.024	0.933	0.895	0.881	0.908	0.937	0.934
ISDU-QSMNet-USW, $K=4$	0.046 ± 0.024	0.041 ± 0.026	0.043 ± 0.022	0.040 ± 0.021	0.064 ± 0.030	0.050 ± 0.023	0.939	0.891	0.884	0.918	0.927	0.935
ISDU-QSMNet-USW-RS, $K=4$	**0.046 ± 0.023**	**0.038 ± 0.026**	0.038 ± 0.021	**0.037 ± 0.021**	0.058 ± 0.029	0.049 ± 0.020	**0.944**	**0.904**	**0.886**	**0.919**	**0.938**	**0.943**
ROI: Putamen												
COSMOS	0.033 ± 0.027	0.047 ± 0.035	0.040 ± 0.028	0.051 ± 0.029	0.070 ± 0.037	0.042 ± 0.025	1	1	1	1	1	1
QSMnet	0.029 ± 0.025	0.043 ± 0.033	**0.039 ± 0.027**	0.044 ± 0.029	0.054 ± 0.035	**0.043 ± 0.027**	0.919	**0.916**	0.933	0.931	0.934	0.912
DeepQSM	0.032 ± 0.026	**0.047 ± 0.032**	0.042 ± 0.027	0.045 ± 0.026	0.056 ± 0.032	0.047 ± 0.025	0.917	0.902	0.922	0.936	0.931	0.896
xQSM	0.032 ± 0.025	0.044 ± 0.031	**0.041 ± 0.027**	0.045 ± 0.026	0.057 ± 0.033	0.046 ± 0.026	0.934	0.906	**0.936**	**0.939**	**0.940**	0.908
LP-CNN	0.047 ± 0.027	0.064 ± 0.034	0.059 ± 0.028	0.064 ± 0.029	0.087 ± 0.035	0.063 ± 0.026	0.909	0.889	0.890	0.898	0.876	0.883
SpiNet-QSM	0.040 ± 0.026	0.047 ± 0.033	0.046 ± 0.027	**0.053 ± 0.027**	0.077 ± 0.035	0.047 ± 0.023	0.938	0.904	0.919	0.925	0.930	0.915
STAR-QSM	0.049 ± 0.030	0.033 ± 0.039	**0.039 ± 0.028**	0.033 ± 0.025	0.050 ± 0.037	0.046 ± 0.024	0.892	0.842	0.850	0.879	0.855	0.867
NDI	0.022 ± 0.023	0.037 ± 0.029	0.031 ± 0.026	0.034 ± 0.026	0.046 ± 0.029	0.036 ± 0.024	0.865	0.874	0.864	0.877	0.866	0.881
MoDL-QSM-SW, $K=4$	0.038 ± 0.026	0.050 ± 0.034	0.049 ± 0.027	0.054 ± 0.029	0.064 ± 0.031	0.051 ± 0.025	0.941	0.913	0.923	0.928	0.929	0.928
ISDU-QSMNet-USW, $K=4$	0.039 ± 0.025	0.052 ± 0.033	0.050 ± 0.027	0.055 ± 0.028	0.074 ± 0.035	0.053 ± 0.024	0.943	0.913	0.934	0.932	0.928	0.927

(Continues)

TABLE 12 | (Continued)

Method	Susceptibility values						Correlation with COSMOS					
	Sub-1	Sub-2	Sub-3	Sub-4	Sub-5	Sub-6	Sub-1	Sub-2	Sub-3	Sub-4	Sub-5	Sub-6
ISDU-QSMNet-USW-RS, $K=4$	**0.034 ± 0.025**	0.045 ± 0.031	0.045 ± 0.025	**0.049 ± 0.026**	**0.073 ± 0.036**	0.047 ± 0.023	**0.946**	0.914	0.935	0.931	0.937	**0.933**
ROI: Globus pallidus												
COSMOS	0.127 ± 0.039	0.152 ± 0.062	0.128 ± 0.046	0.127 ± 0.043	0.166 ± 0.055	0.124 ± 0.038	1	1	1	1	1	1
QSMnet	0.120 ± 0.039	0.136 ± 0.055	0.123 ± 0.046	0.121 ± 0.044	0.134 ± 0.052	0.120 ± 0.041	0.909	0.895	0.948	0.934	0.903	0.925
DeepQSM	0.122 ± 0.037	0.138 ± 0.053	0.126 ± 0.043	0.120 ± 0.039	0.135 ± 0.048	0.120 ± 0.037	0.913	0.896	0.924	0.923	0.910	0.921
xQSM	**0.126 ± 0.038**	0.141 ± 0.052	**0.128 ± 0.045**	0.122 ± 0.041	0.142 ± 0.050	**0.126 ± 0.093**	0.932	0.908	0.947	0.943	0.937	0.926
LP-CNN	0.147 ± 0.042	0.164 ± 0.053	0.151 ± 0.048	0.144 ± 0.048	0.162 ± 0.052	0.146 ± 0.043	0.912	0.897	0.924	0.932	0.899	0.909
SpiNet-QSM	0.138 ± 0.041	**0.154 ± 0.055**	0.135 ± 0.046	0.132 ± 0.043	0.154 ± 0.052	0.130 ± 0.038	**0.945**	**0.937**	0.947	0.954	0.935	0.948
STAR-QSM	0.096 ± 0.037	0.112 ± 0.053	0.105 ± 0.043	0.102 ± 0.040	0.122 ± 0.052	0.102 ± 0.035	0.867	0.868	0.865	0.891	0.823	0.891
NDI	0.086 ± 0.029	0.105 ± 0.041	0.092 ± 0.035	0.089 ± 0.033	0.100 ± 0.037	0.101 ± 0.032	0.860	0.871	0.871	0.860	0.808	0.897
MoDL-QSM-SW, $K=4$	0.140 ± 0.041	0.162 ± 0.057	0.143 ± 0.047	0.141 ± 0.045	0.148 ± 0.051	0.142 ± 0.042	0.943	0.933	0.945	0.952	0.934	0.950
ISDU-QSMNet-USW, $K=4$	0.134 ± 0.039	0.158 ± 0.057	0.137 ± 0.046	0.135 ± 0.045	0.159 ± 0.054	0.134 ± 0.040	0.944	0.932	0.948	**0.957**	0.933	**0.953**
ISDU-QSMNet-USW-RS, $K=4$	0.123 ± 0.038	**0.148 ± 0.054**	0.130 ± 0.045	**0.126 ± 0.042**	**0.163 ± 0.054**	**0.126 ± 0.037**	0.944	**0.937**	**0.951**	0.955	**0.938**	**0.953**
ROI: Left white matter												
COSMOS	−0.010 ± 0.023	−0.007 ± 0.023	−0.005 ± 0.025	−0.008 ± 0.021	−0.009 ± 0.026	−0.007 ± 0.021	1.000	1.000	1.000	1.000	1.000	1.000
SpiNet-QSM	−0.009 ± 0.021	−0.006 ± 0.020	**−0.005 ± 0.024**	−0.009 ± 0.018	**−0.009 ± 0.022**	**−0.007 ± 0.018**	0.932	0.877	0.916	0.889	0.900	0.895
LPCNN-QSM	−0.008 ± 0.021	−0.004 ± 0.018	−0.004 ± 0.023	−0.007 ± 0.017	−0.007 ± 0.022	−0.004 ± 0.018	0.902	0.849	0.895	0.862	0.869	0.882
QSMNet	−0.012 ± 0.020	−0.008 ± 0.018	−0.006 ± 0.022	−0.010 ± 0.018	**−0.009 ± 0.021**	−0.009 ± 0.019	0.924	0.877	0.925	0.902	0.906	0.905
DeepQSM	**−0.010 ± 0.020**	−0.006 ± 0.018	**−0.005 ± 0.022**	**−0.008 ± 0.018**	−0.007 ± 0.021	**−0.007 ± 0.019**	0.918	0.878	0.916	0.891	0.888	0.888
STAR-QSM	−0.007 ± 0.025	−0.003 ± 0.026	−0.002 ± 0.027	−0.005 ± 0.023	−0.006 ± 0.028	−0.004 ± 0.024	0.834	0.814	0.821	0.841	0.821	0.830
NDI	−0.008 ± 0.021	−0.004 ± 0.022	−0.003 ± 0.022	−0.006 ± 0.019	−0.006 ± 0.021	−0.005 ± 0.021	0.860	0.822	0.837	0.830	0.818	0.849
xQSM	−0.011 ± 0.021	**−0.007 ± 0.019**	**−0.005 ± 0.023**	−0.009 ± 0.018	−0.008 ± 0.022	**−0.007 ± 0.019**	0.921	0.880	0.923	0.900	0.891	0.892
MoDL-QSM-SW, $K=4$	**−0.010 ± 0.021**	−0.006 ± 0.019	**−0.005 ± 0.023**	−0.009 ± 0.018	**−0.009 ± 0.022**	−0.006 ± 0.018	0.934	0.885	0.922	0.900	0.910	0.904

(Continues)

TABLE 12 | (Continued)

Method	Susceptibility values						Correlation with COSMOS					
	Sub-1	Sub-2	Sub-3	Sub-4	Sub-5	Sub-6	Sub-1	Sub-2	Sub-3	Sub-4	Sub-5	Sub-6
ISDU-QSMNet-USW, $K=4$	**−0.010 ± 0.022**	−0.006 ± 0.021	−0.004 ± 0.024	**−0.008 ± 0.019**	−0.008 ± 0.023	**−0.007 ± 0.020**	**0.936**	**0.893**	**0.938**	**0.914**	**0.916**	**0.915**
ISDU-QSMNet-USW-RS, $K=4$	−0.009 ± 0.022	−0.003 ± 0.020	−0.003 ± 0.024	−0.006 ± 0.019	−0.007 ± 0.023	−0.004 ± 0.019	0.934	0.884	0.926	0.904	0.909	0.912
ROI: Right white matter												
COSMOS	−0.006 ± 0.032	−0.003 ± 0.026	−0.004 ± 0.028	−0.005 ± 0.030	−0.007 ± 0.034	−0.004 ± 0.028	1.000	1.000	1.000	1.000	1.000	1.000
SpiNet-QSM	−0.005 ± 0.030	−0.004 ± 0.024	−0.003 ± 0.028	**−0.005 ± 0.027**	−0.006 ± 0.030	**−0.004 ± 0.027**	0.945	0.893	0.924	0.927	0.929	0.928
LPCNN-QSM	−0.003 ± 0.031	**−0.003 ± 0.022**	−0.002 ± 0.028	−0.004 ± 0.026	−0.005 ± 0.030	−0.001 ± 0.028	0.923	0.865	0.903	0.903	0.904	0.906
QSMNet	−0.008 ± 0.027	−0.007 ± 0.021	−0.005 ± 0.025	−0.007 ± 0.025	**−0.007 ± 0.027**	−0.006 ± 0.026	0.941	0.889	0.930	0.932	0.927	0.928
DeepQSM	−0.006 ± 0.028	−0.004 ± 0.022	−0.003 ± 0.026	−0.006 ± 0.025	−0.005 ± 0.027	−0.005 ± 0.026	0.935	0.883	0.920	0.926	0.918	0.923
STAR-QSM	−0.003 ± 0.032	−0.002 ± 0.028	−0.001 ± 0.030	−0.002 ± 0.029	−0.005 ± 0.033	−0.002 ± 0.030	0.871	0.823	0.840	0.884	0.841	0.868
NDI	−0.004 ± 0.026	**−0.003 ± 0.023**	−0.003 ± 0.025	−0.003 ± 0.024	−0.005 ± 0.025	−0.003 ± 0.027	0.876	0.820	0.852	0.869	0.835	0.889
xQSM	−0.006 ± 0.028	−0.005 ± 0.022	**−0.004 ± 0.026**	−0.006 ± 0.026	−0.005 ± 0.028	−0.005 ± 0.026	0.937	0.885	0.930	0.927	0.922	0.922
MoDL-QSM-SW, $K=4$	−0.006 ± 0.029	−0.004 ± 0.023	**−0.004 ± 0.026**	**−0.005 ± 0.026**	**−0.007 ± 0.028**	**−0.004 ± 0.025**	0.949	0.902	0.932	0.935	0.938	0.937
ISDU-QSMNet-USW, $K=4$	**−0.006 ± 0.029**	−0.004 ± 0.024	−0.003 ± 0.027	**−0.005 ± 0.027**	−0.005 ± 0.029	**−0.004 ± 0.028**	0.950	**0.908**	**0.941**	**0.939**	0.935	0.938
ISDU-QSMNet-USW-RS, $K=4$	**−0.006 ± 0.030**	−0.004 ± 0.026	−0.003 ± 0.028	−0.004 ± 0.028	−0.006 ± 0.030	**−0.004 ± 0.028**	**0.951**	0.902	0.935	0.937	**0.937**	**0.939**
ROI: Left gray matter												
COSMOS	0.002 ± 0.022	−0.001 ± 0.024	−0.001 ± 0.020	−0.001 ± 0.019	0.002 ± 0.025	−0.001 ± 0.020	1.000	1.000	1.000	1.000	1.000	1.000
SpiNet-QSM	0.001 ± 0.018	0.000 ± 0.019	**−0.001 ± 0.016**	**−0.001 ± 0.015**	0.001 ± 0.019	−0.002 ± 0.016	0.872	0.852	0.847	0.839	0.859	0.857
LPCNN-QSM	**0.002 ± 0.017**	0.001 ± 0.018	0.000 ± 0.015	**−0.001 ± 0.013**	**0.002 ± 0.018**	0.000 ± 0.015	0.829	0.822	0.811	0.796	0.822	0.832
QSMNet	−0.002 ± 0.017	−0.002 ± 0.018	−0.002 ± 0.016	−0.003 ± 0.015	0.000 ± 0.018	−0.004 ± 0.016	0.859	0.838	0.839	0.830	0.865	0.850
DeepQSM	0.000 ± 0.017	**−0.001 ± 0.018**	**−0.001 ± 0.016**	**−0.001 ± 0.015**	0.001 ± 0.018	−0.002 ± 0.016	0.836	0.838	0.832	0.822	0.847	0.842
STAR-QSM	0.004 ± 0.027	0.002 ± 0.027	0.002 ± 0.025	0.003 ± 0.022	0.004 ± 0.028	0.003 ± 0.024	0.756	0.778	0.738	0.786	0.787	0.780
NDI	0.002 ± 0.021	0.001 ± 0.022	0.001 ± 0.020	0.001 ± 0.018	0.003 ± 0.021	0.001 ± 0.021	0.786	0.784	0.763	0.793	0.794	0.812
xQSM	0.000 ± 0.018	**−0.001 ± 0.018**	**−0.001 ± 0.016**	**−0.001 ± 0.015**	0.001 ± 0.019	−0.002 ± 0.016	0.840	0.841	0.838	0.819	0.850	0.831

(Continues)

TABLE 12 | (Continued)

	Susceptibility values						Correlation with COSMOS					
Method	**Sub-1**	**Sub-2**	**Sub-3**	**Sub-4**	**Sub-5**	**Sub-6**	**Sub-1**	**Sub-2**	**Sub-3**	**Sub-4**	**Sub-5**	**Sub-6**
MoDL-QSM-SW, $K=4$	0.001 ± 0.018	0.000 ± 0.019	$\mathbf{-0.001 \pm 0.016}$	$\mathbf{-0.001 \pm 0.015}$	$\mathbf{0.002 \pm 0.019}$	-0.002 ± 0.016	0.871	0.856	0.851	0.841	0.868	0.858
ISDU-QSMNet-USW, $K=4$	$\mathbf{0.002 \pm 0.019}$	$\mathbf{-0.001 \pm 0.020}$	$\mathbf{-0.001 \pm 0.018}$	$\mathbf{-0.001 \pm 0.017}$	0.003 ± 0.020	$\mathbf{-0.001 \pm 0.018}$	0.867	**0.865**	**0.860**	0.847	**0.874**	**0.871**
ISDU-QSMNet-USW-RS, $K=4$	$\mathbf{0.002 \pm 0.018}$	-0.002 ± 0.019	$\mathbf{-0.001 \pm 0.017}$	$\mathbf{-0.001 \pm 0.015}$	0.003 ± 0.020	$\mathbf{-0.001 \pm 0.016}$	**0.875**	0.861	0.859	**0.848**	0.872	0.866
					ROI: Right gray matter							
COSMOS	-0.001 ± 0.022	-0.002 ± 0.024	-0.003 ± 0.019	-0.001 ± 0.022	-0.001 ± 0.025	-0.003 ± 0.019	1.000	1.000	1.000	1.000	1.000	1.000
SpiNet-QSM	0.001 ± 0.018	-0.001 ± 0.018	$\mathbf{-0.003 \pm 0.016}$	$\mathbf{-0.001 \pm 0.017}$	-0.002 ± 0.019	-0.004 ± 0.015	0.865	0.822	0.839	0.848	0.844	0.848
LPCNN-QSM	0.001 ± 0.017	-0.001 ± 0.017	-0.002 ± 0.015	-0.001 ± 0.017	$\mathbf{-0.001 \pm 0.019}$	-0.001 ± 0.015	0.821	0.788	0.810	0.810	0.801	0.820
QSMNet	-0.003 ± 0.018	-0.004 ± 0.017	-0.004 ± 0.016	-0.003 ± 0.017	-0.003 ± 0.018	-0.005 ± 0.016	0.855	0.814	0.838	0.845	0.841	0.847
DeepQSM	-0.002 ± 0.018	$\mathbf{-0.002 \pm 0.017}$	$\mathbf{-0.003 \pm 0.016}$	-0.002 ± 0.017	$\mathbf{-0.001 \pm 0.018}$	-0.004 ± 0.016	0.838	0.800	0.820	0.833	0.832	0.834
STAR-QSM	0.002 ± 0.028	0.000 ± 0.028	0.000 ± 0.024	0.003 ± 0.025	0.001 ± 0.029	0.001 ± 0.024	0.760	0.757	0.718	0.797	0.767	0.773
NDI	0.001 ± 0.021	-0.001 ± 0.023	-0.001 ± 0.020	0.001 ± 0.020	0.000 ± 0.022	-0.001 ± 0.021	0.779	0.782	0.749	0.801	0.771	0.802
xQSM	$\mathbf{-0.001 \pm 0.018}$	$\mathbf{-0.002 \pm 0.017}$	$\mathbf{-0.003 \pm 0.016}$	-0.002 ± 0.017	-0.002 ± 0.018	-0.004 ± 0.016	0.839	0.801	0.830	0.833	0.833	0.831
MoDL-QSM-SW, $K=4$	0.000 ± 0.018	-0.001 ± 0.018	$\mathbf{-0.003 \pm 0.016}$	$\mathbf{-0.001 \pm 0.017}$	-0.002 ± 0.019	-0.004 ± 0.015	0.866	0.831	0.842	0.853	0.853	0.848
ISDU-QSMNet-USW, $K=4$	$\mathbf{-0.001 \pm 0.018}$	-0.001 ± 0.019	-0.002 ± 0.017	$\mathbf{-0.001 \pm 0.019}$	$\mathbf{-0.001 \pm 0.020}$	$\mathbf{-0.003 \pm 0.018}$	**0.868**	0.831	**0.854**	**0.860**	**0.855**	**0.866**
ISDU-QSMNet-USW-RS, $K=4$	0.001 ± 0.019	$\mathbf{-0.002 \pm 0.019}$	-0.001 ± 0.016	0.001 ± 0.018	0.000 ± 0.020	-0.002 ± 0.016	0.866	**0.836**	0.847	0.856	0.854	0.858

TABLE 13 | Ablation study results on the SNU dataset using the full training data. The performance metrics reported include SSIM, pSNR, NRMSE, and HFEN (mean ± standard deviation).

Exp. no.	Unshared weights	Random subset sampling	SSIM	pSNR	NRMSE	HFEN
1	X	X	0.911 ± 0.015	41.221 ± 1.739	50.606 ± 4.371	47.767 ± 5.007
2	X	✓	0.910 ± 0.015	41.127 ± 1.166	51.302 ± 4.354	48.457 ± 5.055
3	✓	X	0.915 ± 0.014	41.367 ± 1.102	50.308 ± 3.865	46.725 ± 5.019
4	✓	✓	**0.916 ± 0.014**	**41.415 ± 1.130**	**49.749 ± 4.133**	**46.562 ± 5.150**

The ISDU-QSMNet model is trained on the SNU dataset, which includes five distinct orientations per subject, along with additional augmented data incorporating arbitrary rotations between -30° and $+30^{\circ}$. While this introduces orientation diversity during training, it is handled implicitly through data-driven learning. The model does not include any explicit formulation or architectural mechanism to ensure orientation invariance. Consequently, although the network has been exposed to a range of orientations, its ability to generalize to unseen or more extreme orientation scenarios remains empirically unproven and lacks theoretical guarantees. This implicit handling of orientation variability represents a limitation of the current approach and highlights the need for future work to incorporate explicit rotation-invariant components or physics-informed constraints to enhance robustness across diverse dipole orientations.

5 | Conclusions

This study introduced ISDU-QSMNet, a novel model-based deep-learning approach for QSM reconstruction. The results demonstrate that the proposed ISDU-QSMNet outperforms existing techniques in full-data training scenarios and matches or exceeds the performance in limited data training situations. The implementation of unshared weights across iterations improved the overall denoising capability, whereas random subset sampling reduced the training time without compromising the accuracy. The model exhibited strong generalization capabilities, and ROI analysis revealed good alignment with the COSMOS reference values. ISDU-QSMNet effectively integrates QSM physics with deep learning capabilities. In conclusion, the ISDU-QSMNet represents an advancement in QSM reconstruction, offering superior performance, efficiency, and generalizability, thus providing a foundation for enhancing QSM applications in research and clinical settings.

Author Contributions

Vaddadi Venkatesh: conceptualization, data curation, formal analysis, investigation, methodology, software, validation, visualization, writing – original draft, and writing - review & editing. **Raji Susan Mathew:** formal analysis, investigation, project administration, validation, and writing – review & editing. **Phaneendra K. Yalavarthy:** formal analysis, funding acquisition, investigation, project administration, resources, supervision, validation, and writing – review & editing.

Acknowledgements

This work was supported by the S. Ramachandran-National Bioscience Award for Career Development awarded by the Department of Biotechnology, Govt. of India, and in part by an ARG Grant# ARG01-0524-230330 from the Qatar National Research Fund (a member of the Qatar Foundation). The authors express their gratitude to Dr. Jongho Lee from the Laboratory for Imaging Science and Technology, Department of Electrical and Computer Engineering, Seoul National University, South Korea, for providing data. The authors also thank Dr. Jeremias Sulam from the Biomedical Engineering Department, Johns Hopkins University, for making their data publicly accessible [39].

Conflicts of Interest

The authors declare no conflicts of interest.

Data Availability Statement

The data that support the findings of this study are openly available in ISDU-QSM Net at https://github.com/venkateshvaddadi/ISDU_QSMNet.

References

1. A. Deistung, F. Schweser, and J. R. Reichenbach, "Overview of Quantitative Susceptibility Mapping," *NMR in Biomedicine* 30, no. 4 (2017): e3569.

2. F. Schweser, A. Deistung, and J. R. Reichenbach, "Foundations of MRI Phase Imaging and Processing for Quantitative Susceptibility Mapping (QSM)," *Zeitschrift für Medizinische Physik* 26, no. 1 (2016): 6–34.

3. C. Liu, H. Wei, N. J. Gong, M. Cronin, R. Dibb, and K. Decker, "Quantitative Susceptibility Mapping: Contrast Mechanisms and Clinical Applications," *Tomography* 1, no. 1 (2015): 3–17.

4. J. Reichenbach, F. Schweser, B. Serres, and A. Deistung, "Quantitative Susceptibility Mapping: Concepts and Applications," *Clinical Neuroradiology* 25, no. 2 (2015): 225–230.

5. F. Yan, N. He, and E. M. Haacke, "Quantitative Susceptibility Mapping in Neurodegeneration," *Frontiers in Neuroscience* 15 (2021): 724550, https://doi.org/10.3389/fnins.2021.724550.

6. P. Ravanfar, S. M. Loi, W. T. Syeda, et al., "Systematic Review: Quantitative Susceptibility Mapping (QSM) of Brain Iron Profile in Neurodegenerative Diseases," *Frontiers in Neuroscience* 15 (2021): 618435.

7. P. M. Cogswell and A. P. Fan, "Multimodal Comparisons of QSM and PET in Neurodegeneration and Aging," *NeuroImage* 273 (2023): 120068, https://doi.org/10.1016/j.neuroimage.2023.120068.

8. C. Langkammer, L. Pirpamer, S. Seiler, et al., "Quantitative Susceptibility Mapping in Parkinson's Disease," *PLoS ONE* 11, no. 9 (2016): e0162460.

9. A. Alkemade, d G. Hollander, M. C. Keuken, et al., "Comparison of T2*-Weighted and QSM Contrasts in Parkinson's Disease to Visualize the STN With MRI," *PLoS ONE* 12, no. 4 (2017): e0176130.

10. C. Langkammer, F. Schweser, N. Krebs, et al., "Quantitative Susceptibility Mapping (QSM) as a Means to Measure Brain Iron? A Post Mortem Validation Study," *NeuroImage* 62, no. 3 (2012): 1593–1599.

11. J. Acosta-Cabronero, G. B. Williams, A. Cardenas-Blanco, R. J. Arnold, V. Lupson, and P. J. Nestor, "In Vivo Quantitative Susceptibility Mapping (QSM) in Alzheimer's Disease," *PLoS ONE* 8, no. 11 (2013): e81093.

12. Y. Uchida, H. Kan, K. Sakurai, K. Oishi, and N. Matsukawa, "Quantitative Susceptibility Mapping as an Imaging Biomarker for Alzheimer's Disease: The Expectations and Limitations," *Frontiers in Neuroscience* 16 (2022): 938092.

13. P. M. Cogswell, H. J. Wiste, M. L. Senjem, et al., "Associations of Quantitative Susceptibility Mapping With Alzheimer's Disease Clinical and Imaging Markers," *NeuroImage* 224 (2021): 117433.

14. K. M. Gillen, M. Mubarak, C. Park, et al., "QSM Is an Imaging Biomarker for Chronic Glial Activation in Multiple Sclerosis Lesions," *Annals of Clinical and Translational Neurology* 8, no. 4 (2021): 877–886.

15. M. Tranfa, G. Pontillo, M. Petracca, et al., "Quantitative MRI in Multiple Sclerosis: From Theory to Application," *American Journal of Neuroradiology* 43, no. 12 (2022): 1688–1695.

16. C. Wisnieff, S. Ramanan, J. Olesik, S. Gauthier, Y. Wang, and D. Pitt, "Quantitative Susceptibility Mapping (QSM) of White Matter Multiple Sclerosis Lesions: Interpreting Positive Susceptibility and the Presence of Iron," *Magnetic Resonance in Medicine* 74, no. 2 (2015): 564–570.

17. E. M. Haacke, S. Liu, S. Buch, W. Zheng, D. Wu, and Y. Ye, "Quantitative Susceptibility Mapping: Current Status and Future Directions," *Magnetic Resonance Imaging* 33, no. 1 (2015): 1–25.

18. J. Liu, T. Liu, d L. Rochefort, et al., "Morphology Enabled Dipole Inversion for Quantitative Susceptibility Mapping Using Structural Consistency Between the Magnitude Image and the Susceptibility Map," *NeuroImage* 59, no. 3 (2012): 2560–2568.

19. C. Milovic, B. Bilgic, B. Zhao, J. Acosta-Cabronero, and C. Tejos, "Fast Nonlinear Susceptibility Inversion With Variational Regularization," *Magnetic Resonance in Medicine* 80, no. 2 (2018): 814–821.

20. D. Polak, I. Chatnuntawech, J. Yoon, et al., "Nonlinear dipole inversion (NDI) enables robust quantitative susceptibility mapping (QSM)," *NMR in Biomedicine* 33, no. 12 (2020): e4271.

21. T. Liu, P. Spincemaille, L. De Rochefort, B. Kressler, and Y. Wang, "Calculation of Susceptibility Through Multiple Orientation Sampling (COSMOS): A Method for Conditioning the Inverse Problem From Measured Magnetic Field Map to Susceptibility Source Image in MRI," *Magnetic Resonance in Medicine* 61, no. 1 (2009): 196–204.

22. J. Yoon, E. Gong, I. Chatnuntawech, et al., "Quantitative Susceptibility Mapping Using Deep Neural Network: QSMnet," *NeuroImage* 179 (2018): 199–206.

23. O. Ronneberger, P. Fischer, and T. Brox, *U-net: Convolutional Networks for Biomedical Image Segmentation* (Springer, 2015), 234–241.

24. S. Bollmann, K. G. B. Rasmussen, M. Kristensen, et al., "DeepQSM-Using Deep Learning to Solve the Dipole Inversion for Quantitative Susceptibility Mapping," *NeuroImage* 195 (2019): 373–383.

25. Y. Gao, X. Zhu, B. A. Moffat, et al., "XQSM: Quantitative Susceptibility Mapping With Octave Convolutional and Noise-Regularized Neural Networks," *NMR in Biomedicine* 34, no. 3 (2021): e4461, https://doi.org/10.1002/nbm.4461.

26. H. K. Aggarwal, M. P. Mani, and M. Jacob, "MoDL: Model-Based Deep Learning Architecture for Inverse Problems," *IEEE Transactions on Medical Imaging* 38, no. 2 (2018): 394–405.

27. Z. Xiong, Y. Gao, F. Liu, and H. Sun, "*Affine* Transformation Edited and Refined Deep Neural Network for Quantitative Susceptibility Mapping," *NeuroImage* 267 (2023): 119842.

28. S. Graf, W. A. Wohlgemuth, and A. Deistung, "Incorporating A-priori Information in Deep Learning Models for Quantitative Susceptibility Mapping via Adaptive Convolution," *Frontiers in Neuroscience* 18 (2024): 1366165.

29. G. Oh, H. Bae, H. S. Ahn, S. H. Park, W. J. Moon, and J. C. Ye, "Unsupervised Resolution-Agnostic Quantitative Susceptibility Mapping Using Adaptive Instance Normalization," *Medical Image Analysis* 79 (2022): 102477.

30. Y. Gao, Z. Xiong, A. Fazlollahi, et al., "Instant Tissue Field and Magnetic Susceptibility Mapping From MRI Raw Phase Using Laplacian Enhanced Deep Neural Networks," *NeuroImage* 259 (2022): 119410.

31. Y. Gao, Z. Xiong, S. Shan, et al., "Plug-and-Play Latent Feature Editing for Orientation-Adaptive Quantitative Susceptibility Mapping Neural Networks," *Medical Image Analysis* 94 (2024): 103160.

32. N. Paluru, R. Susan Mathew, and P. K. Yalavarthy, "DF-QSM: Data Fidelity Based Hybrid Approach for Improved Quantitative Susceptibility Mapping of the Brain," *NMR in Biomedicine* 37 (2024): e5163.

33. J. Zhang, Z. Liu, S. Zhang, et al., "Fidelity Imposed Network Edit (FINE) for Solving Ill-Posed Image Reconstruction," *NeuroImage* 211 (2020): 116579.

34. R. S. Mathew, N. Paluru, and P. K. Yalavarthy, "Model Resolution-Based Deconvolution for Improved Quantitative Susceptibility Mapping," *NMR in Biomedicine* 37, no. 2 (2024): e5055.

35. Z. Xiong, Y. Gao, Y. Liu, et al., "Quantitative Susceptibility Mapping Through Model-Based Deep Image Prior (MoDIP)," *NeuroImage* 291 (2024): 120583.

36. S. Liang, E. Bell, Q. Qu, R. Wang, and S. Ravishankar, "Analysis of Deep Image Prior and Exploiting Self-Guidance for Image Reconstruction," *IEEE Transactions on Computational Imaging* 11 (2025): 435–451.

37. P. Chakrabarty and S. Maji, "The Spectral Bias of the Deep Image Prior". arXiv preprint arXiv:1912.08905 (2019).

38. Y. Cheng, T. Zeng, P. Lio, C. B. Schönlieb, A. I. Aviles-Rivero, "Deep Spectral Prior". arXiv preprint arXiv:2505.19873 (2025).

39. K. W. Lai, M. Aggarwal, v P. Zijl, X. Li, and J. Sulam, *Learned Proximal Networks for Quantitative Susceptibility Mapping* (Springer, 2020), 125–135.

40. V. Venkatesh, R. S. Mathew, and P. K. Yalavarthy, "Spinet-QSM: Model-Based Deep Learning With Schatten P-Norm Regularization for Improved Quantitative Susceptibility Mapping," *Magnetic Resonance Materials in Physics, Biology and Medicine* 37 (2024): 1–427.

41. C. Langkammer, F. Schweser, K. Shmueli, et al., "Quantitative Susceptibility Mapping: Report From the 2016 Reconstruction Challenge," *Magnetic Resonance in Medicine* 79, no. 3 (2018): 1661–1673.

42. J. P. Marques, J. Meineke, C. Milovic, et al., "QSM Reconstruction Challenge 2.0: A Realistic in Silico Head Phantom for MRI Data Simulation and Evaluation of Susceptibility Mapping Procedures," *Magnetic Resonance in Medicine* 86, no. 1 (2021): 526–542.

43. Committee QCO, B. Bilgic, C. Langkammer, et al., "QSM Reconstruction Challenge 2.0: Design and Report of Results," *Magnetic Resonance in Medicine* 86, no. 3 (2021): 1241–1255.

44. R. Feng, J. Zhao, H. Wang, et al., "MoDL-QSM: Model-Based Deep Learning for Quantitative Susceptibility Mapping," *NeuroImage* 240 (2021): 118376.

45. K. He, X. Zhang, S. Ren, J. Sun, Deep Residual Learning for Image Recognition. (2016): 770–778.

46. P. A. Yushkevich, Y. Gao, G. Gerig, "ITK-SNAP: An Interactive Tool for Semi-Automatic Segmentation of Multimodality Biomedical Images" IEEE 2016 3342 3345

47. B. Billot, D. N. Greve, O. Puonti, et al., "Synthseg: Segmentation of Brain MRI Scans of any Contrast and Resolution Without Retraining," *Medical Image Analysis* 86 (2023): 102789, https://doi.org/10.1016/j.media.2023.102789.

Supporting Information

Additional supporting information can be found online in the Supporting Information section. **Table S1:** Comparison of susceptibility values (in ppm) and their correlations with COSMOS across the following eight ROIs: caudate (CAU), putamen (PUT), globus pallidus (GP), left/right white matter (WM), and left/right gray matter (GM), derived from reconstructed susceptibility maps for six test subjects from the SNU dataset. All models were trained on limited training data from SNU dataset. For each subject's ROI, the best-performing method (i.e., susceptibility value with the smallest deviation from COSMOS and highest correlation coefficient) is highlighted in bold. **Figure S1:** An example susceptibility image reconstructed from RC-1 data using models trained on the full dataset using SNU dataset. The first row shows the reference COSMOS maps in the following three orthogonal views: sagittal, coronal, and axial. Each subsequent row shows reconstructions from a different method: SpiNet-QSM, LPCNN, QSMnet, DeepQSM, xQSM, ISDU-QSMNet-USW, and ISDU-QSMNet-USW-RS. Each model row displays the same three views and includes quantitative evaluation metrics as x-axis labels—structural similarity index measure (SSIM), peak signal-to-noise ratio (PSNR), and high-frequency error norm (HFEN)—computed with respect to the COSMOS reference. **Figure S2:** An example susceptibility image reconstructed from LPCNN data using models trained on the full dataset using SNU dataset. The first row shows the reference COSMOS maps in the following three orthogonal views: sagittal, coronal, and axial. Each subsequent row shows reconstructions from a different method: SpiNet-QSM, LPCNN, QSMnet, DeepQSM, xQSM, ISDU-QSMNet-USW, and ISDU-QSMNet-USW-RS. Each model row displays the same three views and includes quantitative evaluation metrics as x-axis labels—structural similarity index measure (SSIM), peak signal-to-noise ratio (PSNR), and high-frequency error norm (HFEN)—computed with respect to the COSMOS reference. **Figure S3:** Comparison of quantitative susceptibility mapping (QSM) reconstructions for subject 7 from the SNU dataset, across multiple models trained with the SNU dataset with full training data settings. The first row shows the reference COSMOS maps in the following three orthogonal views: sagittal, coronal, and axial. Each subsequent row shows reconstructions from a different method: SpiNet-QSM, LPCNN, QSMnet, DeepQSM, xQSM, ISDU-QSMNet-USW, and ISDU-QSMNet-USW-RS. Each model row displays the same three views and includes quantitative evaluation metrics asx-axis labels—structural similarity index measure (SSIM), peak signal-to-noise ratio (PSNR), and HFEN (HFEN)—computed with respect to the COSMOS reference. **Figure 4:** Comparison of quantitative susceptibility mapping (QSM) reconstructions for subject-8 from the SNU dataset, across multiple models trained with the SNU dataset with full training data settings. The first row shows the reference COSMOS maps in the following three orthogonal views: sagittal, coronal, and axial. Each subsequent row shows reconstructions from a different method: SpiNet- QSM, LPCNN, QSMnet, DeepQSM, xQSM, ISDU-QSMNet-USW, and ISDU-QSMNet-USW-RS. Each model row displays the same three views and includes quantitative evaluation metrics asx-axis labels—structural similarity index measure (SSIM), peak signal-to-noise ratio (PSNR), and HFEN (HFEN)—computed with respect to the COSMOS reference. **Figure 5:** Comparison of quantitative susceptibility mapping (QSM) reconstructions for subject-9 from the SNU dataset, across multiple models trained with the SNU dataset with full training data settings. The first row shows the reference COSMOS maps in the following three orthogonal views: sagittal, coronal, and axial. Each subsequent row shows reconstructions from a different method: SpiNet- QSM, LPCNN, QSMnet, DeepQSM, xQSM, ISDU-QSMNet-USW, and ISDU-QSMNet-USW-RS. Each model row displays the same three views and includes quantitative evaluation metrics as x-axis labels—structural similarity index measure (SSIM), peak signal-to-noise ratio (PSNR), and high-frequency error norm (HFEN)—computed with respect to the COSMOS reference. **Figure 6:** Sample QSM reconstructions for Subject 8 from the SNU dataset, obtained using the proposed ISDU-QSMNet with different denoising networks: Simple Wide ResNet CNN, UNet-mini, UNet-heavy, and WideResNet-18. WideResNet-18 demonstrates the best reconstruction quality, leading to its selection as the denoising network for ISDU-QSMNet.